

A Scalar Anisotropy Model for Turbulent Eddy Viscosity

Scott M. Murman

Scott.M.Murman@nasa.gov

NASA Ames Research Center, Moffett Field, CA, USA

Abstract

A three-equation eddy-viscosity turbulence model using transport equations for the turbulent kinetic energy (k), dissipation rate (ϵ), and a scalar measure of the Reynolds-stress anisotropy is described. Away from walls, where the turbulence anisotropy goes to zero, the model naturally reverts to the isotropic k - ϵ formulation, with only a slightly modified value of the eddy-viscosity coefficient. This leverages the predictive capability of k - ϵ for free shear flows, while still providing accurate predictions of wall-bounded flows without resorting to wall-damping functions. The computed model predictions are compared against experimental Reynolds-stress measurements for a zero-pressure-gradient flat-plate boundary layer, a planar mixing-layer, and the separated flow over periodic hills. Further, the computed results show improvements over standard one- and two-equation models, most notably for the smooth-body separation and recirculation encountered in the flow over periodic hills.

Keywords: v^2 - f , SSG, pressure-strain, separation

Nomenclature

σ_ϵ	1.3
σ_φ	1.3
σ_k	1.0
C_1	1.7
C_2	0.9
C_3	0.0
C_μ	0.11
C_{ϵ_1}	1.44

C_{ϵ_2}	1.92
Pr_T	0.9
Re_T^*	2000
β	inviscid blocking function
ϵ	turbulent dissipation rate of k
ϵ_{ij}	turbulent dissipation rate tensor
η_{III}, ξ_{III}	scaled invariants of the Reynolds-stress anisotropy tensor
μ_t	turbulent eddy viscosity
ω	turbulent specific dissipation rate
Φ_{ij}	turbulent pressure-strain
Π_{ij}	turbulent velocity pressure correlation
φ	scalar Reynolds-stress anisotropy
ξ	anisotropy velocity scale
a_{ij}	Reynolds-stress anisotropy tensor = $\frac{\langle u'_i u'_j \rangle}{k} - \frac{2}{3} \delta_{ij}$
C_μ^*	anisotropic eddy-viscosity coefficient
D_{ij}	turbulent diffusion
e_{ij}	anisotropy of the turbulent dissipation rate tensor = $\frac{\epsilon_{ij}}{\epsilon} - \frac{2}{3} \delta_{ij}$
f	scalar elliptic relaxation
k	turbulent kinetic energy = $\langle u'_i u'_i \rangle / 2$
L	turbulent length scale
P_{ij}	turbulent production
Re_τ	channel friction Reynolds number = $\frac{u_\tau H}{\nu}$
Re_b	channel bulk Reynolds number
Re_T	turbulence Reynolds number = $\frac{k^2}{\epsilon \nu}$
S^*	compressible strain rate
T	turbulent time scale
Tu	turbulence intensity
v^2	wall-normal turbulent Reynolds stress = $\langle u'_2 u'_2 \rangle$
λ	dilatational viscosity coefficient = $-2/3 \mu$
μ	shear viscosity coefficient
ρ	density
θ	temperature
E	total energy
e	internal energy

f	inviscid flux vector
g	viscous flux vector
H	periodic hill height
h	source term
q	conserved variables
t	time
u	velocity
u_τ	friction velocity
u_b	channel bulk velocity
∞	freestream
Ω, Γ	domain
n	normal direction
w	wall
$\langle \rangle$	averaging operator
$'$	fluctuating component - unprimed quantities are averages

1 Introduction

Extending turbulence models for the Reynolds-averaged Navier-Stokes (RANS) equations to provide robust engineering predictions for complex flows, *e.g.* flows with separation and reattachment, plume interactions, strong curvature, *etc.*, has proven difficult. Results from the recent Drag Prediction Workshop series[1, 2] and NASA’s Constellation Program[3, 4] document the inconsistent predictions of “state-of-the-art” RANS turbulence models when encountering even relatively mild separation. Broadly generalizing, two approaches for addressing this problem are identifiable. In the first, known deficiencies in existing, well-understood models are corrected to extend their applicability and accuracy, *e.g.* curvature and compressibility corrections, realizability, numerical robustness. By rectifying known deficiencies, it is expected that the error in predicting unanticipated flow structures will decrease. This approach has mainly focused on the Spalart-Allmaras (SA)[5] and Shear-Stress-Transport (SST)[6] models, given their success in industrial high-Reynolds-number Computational Fluid Dynamics (CFD) applications. The second approach uses higher-moment Reynolds-stress terms, in either algebraic or differential form, to increase the fidelity of the physical representation with the model, at the acknowledged cost of increasing model complexity (*cf.* [7–10]). This approach is less mature than the former, for many reasons, but

has demonstrated commensurate accuracy for some practical problems. Both approaches have strengths and weaknesses, but neither to-date produces consistent quantitative predictions when encountering complex flows outside the models scope of calibration.

The current work is motivated by Durbin’s v^2 - f model[11], both from the standpoint of improving existing linear eddy-viscosity models, and as an incremental step towards full Reynolds-stress modeling. The v^2 - f model augments the standard k - ϵ turbulence model[12, 13] using the wall-normal Reynolds-stress (v^2), and a non-local wall pressure-blocking term (f) based on the idea of elliptic relaxation. This combination effectively replaces the need for low-Reynolds-number wall damping in the k - ϵ equations with an extensible, physically motivated approach which has shown promise for recirculating flows[14, 15].

Several modifications for the v^2 - f model have been proposed since its introduction[15–22]. These changes are primarily aimed at adjusting the model coefficients, and improving the numerical properties of the elliptic relaxation near the wall. The current work maintains the key ideas of the v^2 - f model - incorporating Reynolds-stress anisotropy in the eddy-viscosity formulation and a wall blocking effect - but in a form which improves the applicability of the model for complex problems in external aerodynamics. Specifically, the v^2 - f model does not naturally revert to the k - ϵ formulation in the absence of wall blocking. The k - ϵ model provides accurate predictions for many free shear flows, and compatibility between v^2 - f and k - ϵ is a desire that the model naturally returns to a self-consistent model away from the influence of walls. Most implementations of v^2 - f include at least one nonlinear model coefficient in an attempt to reconcile this incompatibility. Further, Davidson *et al.* [19] have demonstrated that limiting the v^2 - f eddy-viscosity formulation to the k - ϵ value improves the model predictions for channel flow. The approach here develops a nonlinear eddy-viscosity formulation that naturally blends the two models. The philosophy is to develop the model as much as possible from fundamental idealized flows, *e.g.* isotropic turbulence, homogenous shear, *etc.*, as with the original k - ϵ formulation, rather than tuning coefficients to specific flow regimes. In this manner it is hoped that the model will reasonably extend to more complex situations, which involve interactions between fundamental flows, rather than be valid only for specific calibration cases.

This work begins with a development of the model outlined above in Sec. 2, followed by demonstration cases - a zero-pressure-gradient flat-plate boundary layer, a planar mixing-layer, and the separated flow over an array of hills (Sec. 3). The model has been evaluated for other benchmark channel and diffuser flows, but the subset of computations presented here are representative of these simulations. The computed results are compared against both

experimental data and the results of standard implementations for the SA and SST models. A qualitative comparison against a standard implementation of the v^2 - f model from the literature is included for the periodic hills simulation. The paper closes with a summary of the model features and applicability in Sec. 4.

2 Model Development

The compressible RANS equations are written in strong conservation form using Favré, or mass-weighted, ensemble averaging[23]

$$\frac{d}{dt} \int q_l d\Omega + \oint (f_{lj} - g_{lj}) n_j d\Gamma = \int h_l d\Omega, \quad \Gamma = \partial\Omega \quad (1)$$

where q_l are the conserved quantities and f_l is the inviscid flux,

$$q_l = \begin{pmatrix} \rho \\ \rho u_k \\ \rho E \end{pmatrix}, \quad f_{lj} n_j = \begin{pmatrix} \rho u_n \\ \rho u_k u_n + p n_k \\ \rho E u_n + p u_n \end{pmatrix}, \quad u_n = u_j n_j$$

with $\rho E = \rho e + \frac{1}{2} \rho u_k u_k + \rho k$, and an ideal gas equation of state.

The viscous flux, g_{lj} , is given by

$$g_{lj} = Re_{\text{ref}}^{-1} \begin{pmatrix} 0 \\ \tau_{ij} + t_{ij} \\ u_i (\tau_{ij} + t_{ij}) + Pr_{\text{ref}}^{-1} Ec_{\text{ref}}^{-1} \kappa \theta_{,j} - \rho \langle u' E' \rangle \end{pmatrix} \quad (2)$$

$$\tau_{ij} = \mu (u_{i,j} + u_{j,i}) + \lambda u_{k,k} \delta_{ij} - \frac{2}{3} \rho k \delta_{ij} \quad (3)$$

$$t_{ij} = - \langle \rho u'_i u'_j \rangle \quad (4)$$

The source term, h_l , is typically zero, but is activated in the periodic hill numerical experiment, as described in Sec. 3.3. The non-dimensional groups are the reference flow Reynolds number, Prandtl number for the fluid, and the Eckert number, respectively

$$Re_{\text{ref}} = \frac{\rho_{\text{ref}} u_{\text{ref}} L_{\text{ref}}}{\mu_{\text{ref}}}, \quad Pr_{\text{ref}} = \frac{\mu_{\text{ref}} c_{p_{\text{ref}}}}{\kappa_{\text{ref}}}, \quad Ec_{\text{ref}} = \frac{u_{\text{ref}}^2}{c_{p_{\text{ref}}} T_{\text{ref}}}$$

Closure of Eqn. 1 is obtained using an eddy-viscosity model,

$$t_{ij} \simeq \mu'_t u_{i,j} \quad \mu'_t = \frac{\mu_t}{Re_{ref}} \quad (5)$$

$$-\rho \langle u' E' \rangle \simeq \kappa_t \theta_{,j} \quad \kappa_t = \frac{\mu_t}{Pr_T} \quad (6)$$

where the molecular diffusion and turbulent transport of k in the energy equation are assumed negligible outside the hypersonic regime. To both simplify the notation and clarify the relationship to existing models, the turbulence closure is developed using a pseudo-compressible formulation, *i.e.* density is allowed to vary but the turbulence quantities use unweighted ensemble averaging. Extension of the model for high-speed compressible flows is left for future work.

Recognizing the importance of the anisotropy of the Reynolds stress near a solid boundary, Durbin[11] postulated that the appropriate velocity scale (squared) for a linear eddy-viscosity model near the wall is the wall-normal Reynolds-stress, $v^2 = \langle u'_2 u'_2 \rangle$. The eddy viscosity is then given by

$$\mu'_t = C_\mu \rho v^2 T \quad (7)$$

where $T = \frac{k}{\epsilon}$ is the turbulent timescale. Several efforts have proposed similar algebraic corrections to include Reynolds-stress anisotropy information in an eddy-viscosity formulation (*cf.* [24–26]). Further, Hanjalic *et al.* [20] and Laurence *et al.* [21, 22] reformulate the v^2 - f system using the ratio $\frac{v^2}{k}$ as a dependent variable, with the aim of reducing the numerical stiffness in the elliptic relaxation near the wall, while maintaining Eqn. 7 for the eddy viscosity.

Introducing a scalar measure of the flow anisotropy*, $\varphi \simeq \frac{2}{3} - \frac{v^2}{k}$, and following similar arguments, the eddy viscosity is here written as the difference of an isotropic and anisotropic contribution

$$\mu'_t = C_\mu \rho k T - C_\mu^* \rho \varphi k T \quad (8)$$

The anisotropic eddy-viscosity coefficient is assumed to vary linearly with the anisotropy variable φ . The two coefficients of this linear relationship are determined from the limiting

*The Reynolds-stress anisotropy is commonly expressed as $a_{ij} = \frac{\langle u'_i u'_j \rangle}{k} - \frac{2}{3} \delta_{ij}$, so that $\varphi \simeq -a_{22}$. The use of the φ symbol emphasizes that the scalar anisotropy is interpreted here as a modeled quantity. The sign is chosen so that Eqn. 8 is a difference of terms.

values

$$\text{isotropic: } \varphi = 0 \quad \Rightarrow \quad C_\mu^* = 0 \quad (9)$$

$$\text{two-component(wall): } \varphi = \frac{2}{3} \quad \Rightarrow \quad \mu'_t = 0 \quad (10)$$

leading to

$$\mu'_t = C_\mu \rho k T \left[1 - \left(\frac{3}{2} \varphi \right)^2 \right] = C_\mu \rho \xi^2 T, \quad \varphi \in [-2/3, 2/3] \quad (11)$$

with $\xi^2 = k \left[1 - \left(\frac{3}{2} \varphi \right)^2 \right]$ the square of the anisotropic velocity scale. The current model is referred to as the ξ^2 - ϵ model hereafter. Physically the anisotropy can extend to $\varphi = -4/3$, however the lower bound is limited here to maintain $\mu'_t \geq 0$. As we will see, this means there are realizable turbulence states that the current model cannot reproduce, though it does capture the most common situations.

As shown in Fig. 1, Eqn. 11 provides a natural extension of the k - ϵ (piecewise-constant) and v^2 - f (linear) formulations for the eddy-viscosity coefficient. The quadratic variation with anisotropy provides damping in the near-wall region and blends with the original k - ϵ model in isotropic flow without requiring reformulation of the k - ϵ system. The choice of C_μ will be described subsequently. Davidson *et al.* [19] use a piecewise linear combination of the v^2 - f and k - ϵ formulations. The eddy-viscosity formulations are evaluated in *a priori* testing using the DNS channel flow data of Moser *et al.* [27] in Fig. 2. As designed, the ξ^2 - ϵ formulation blends the behavior of the v^2 - f model in the near-wall region with the k - ϵ formulation near the channel centerline. The limiting values of the anisotropy variable determine the numerical boundary conditions, $\varphi|_w = 2/3$ and $\varphi|_\infty = 0$, at the solid boundary and isotropic farfield respectively.

In addition to the standard k and ϵ transport equations[12, 13], to determine the eddy viscosity an equation for the scalar anisotropy is developed from the (incompressible) transport of the Reynolds-stress anisotropy tensor

$$d_t a_{ij} = \frac{P_{ij}}{k} - \left(a_{ij} + \frac{2}{3} \delta_{ij} \right) \frac{P}{k} + a_{ij} \frac{\epsilon}{k} - \frac{1}{k} \left(\epsilon_{ij} - \frac{2}{3} \epsilon \delta_{ij} \right) + \frac{\Pi_{ij}}{k} + \frac{D_{ij}}{k} \quad (12)$$

where d_t represents the total derivative. In the high-Reynolds-number limit where dissipation is isotropic, $\epsilon_{ij} \rightarrow \frac{2}{3} \epsilon \delta_{ij}$, while near a solid boundary the dissipation is strongly anisotropic. This suggests the approximation $e_{ij} = \frac{\epsilon_{ij}}{\epsilon} - \frac{2}{3} \delta_{ij} \parallel a_{ij}$, or that the anisotropy of dissipation is aligned with the anisotropy of Reynolds stress. The angle between the principal directions of

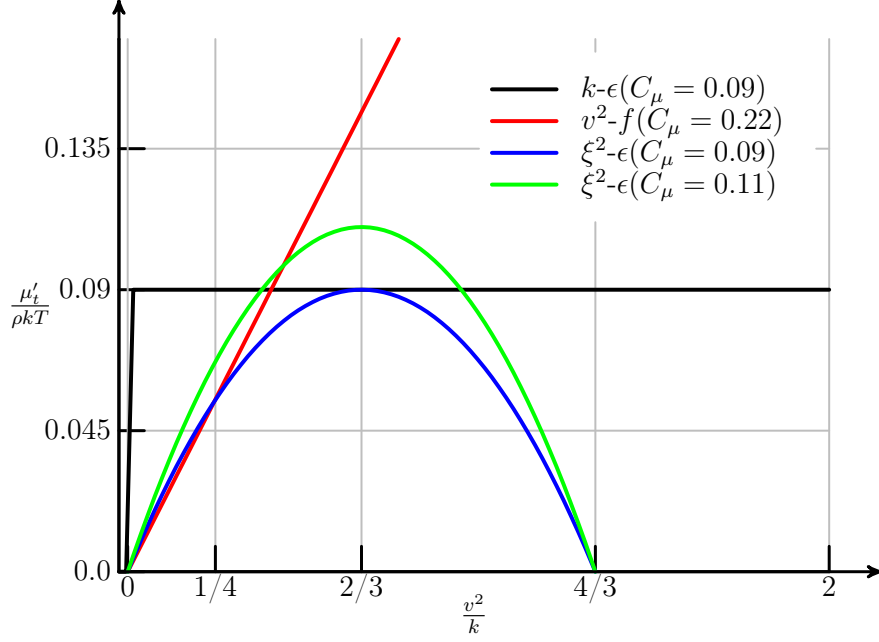


Figure 1: Variation of non-dimensional eddy-viscosity with flow anisotropy. The $v^2 - f$ formulation continues linearly outside the range of the ordinate on the plot.

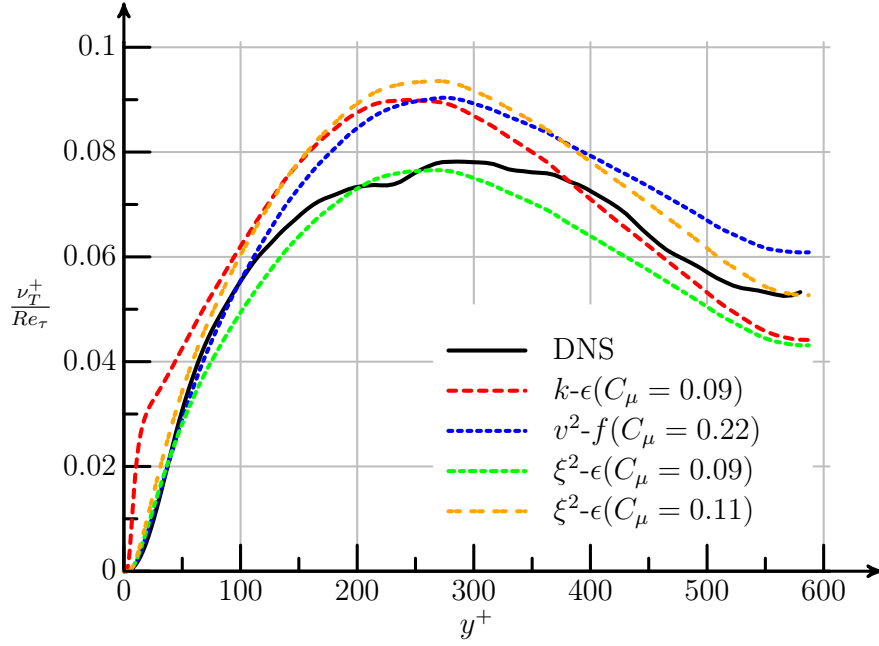


Figure 2: *A priori* testing of the eddy-viscosity formulations using the DNS channel flow data of Moser *et al.* [27] at $Re_\tau = 590$.

the dissipation and Reynolds stress anisotropy tensors are evaluated using the DNS channel flow data in Fig. 3. The alignment of the two tensors is very good through the attached boundary layer. From this we have

$$a_{ij} \frac{\epsilon}{k} - \frac{1}{k} \left(\epsilon_{ij} - \frac{2}{3} \epsilon \delta_{ij} \right) \simeq \beta_\epsilon a_{ij} \frac{\epsilon}{k} \quad (13)$$

where β_ϵ is a model function having the properties

$$\lim_{Re_T \rightarrow 0} \beta_\epsilon = 0 \quad \lim_{Re_T \rightarrow \infty} \beta_\epsilon = 1 \quad (14)$$

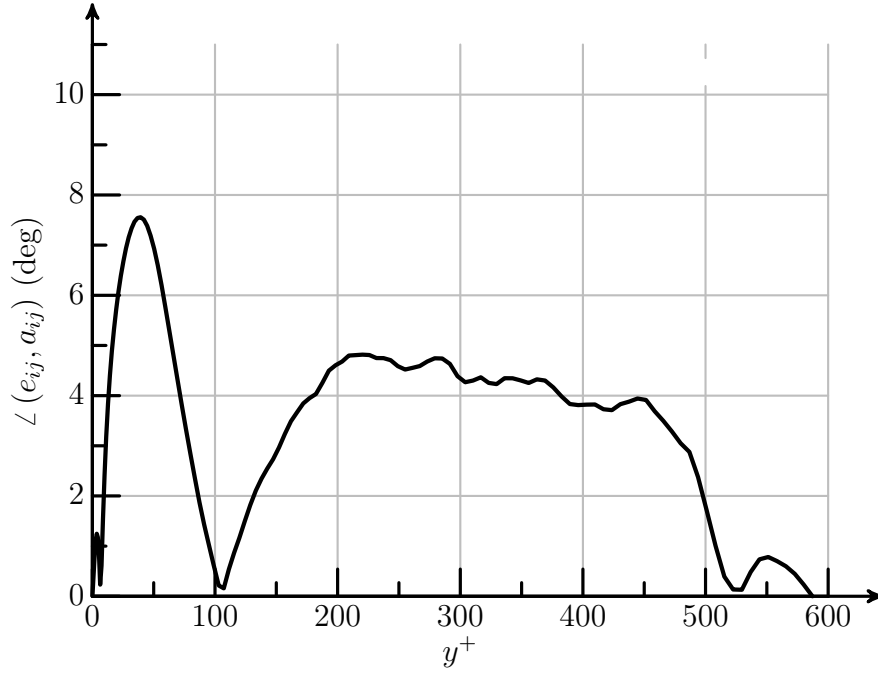


Figure 3: Angle between the principal directions of the dissipation and Reynolds stress anisotropy tensors from the DNS channel flow data of Moser *et al.* [27] at $Re_\tau = 590$.

As is common, the pressure-velocity correlation is split into separate pressure-strain (Φ_{ij}) and pressure-diffusion contributions (D_{ij}^p). The homogeneous pressure-strain model of Speziale *et al.* (SSG)[28] is used here, giving

$$d_t a_{ij} = \frac{P_{ij}}{k} - \left(a_{ij} + \frac{2}{3} \delta_{ij} \right) \frac{P}{k} + \beta_\epsilon a_{ij} \frac{\epsilon}{k} + \beta_\Phi \frac{\Phi_{ij}^h}{k} + \frac{D_{ij}}{k} + \frac{D_{ij}^p}{k} \quad (15)$$

where β_Φ is a functional modification to account for inhomogeneity in the pressure-strain. As we will see, β_Φ has a very similar limit behavior to β_ϵ . Here the convenience of $\beta_\epsilon = \beta_\Phi = \beta$ is adopted. Given the demonstrated success of v^2 - f formulations in the literature using a similar approach (arrived at through different assumptions), this seems a reasonable starting point, though it is perhaps not possible to rigorously justify.

We choose the second component of the Reynolds stress to represent the direction normal to a wall or shear layer. Extracting this component from Eqn. 15, and using a standard gradient-diffusion approach to model the diffusion terms gives

$$d_t(\rho\varphi) - \partial_j \left[Re_{ref}^{-1} \left(\mu + \frac{\mu_t}{\sigma_\varphi} \right) \varphi_{,j} \right] = \frac{\hat{P}_{22}}{k} + \left(\frac{2}{3} - \varphi \right) \frac{P}{k} - \beta \frac{\hat{\Phi}_{22}}{k} \quad (16)$$

where $\hat{\Phi}_{22}$ combines the dissipation and the pressure-strain model*

$$\frac{\hat{\Phi}_{22}}{k} = \frac{C_1 - 1}{T} \rho\varphi + C_2 \varphi \frac{P}{k} - C_3 \frac{P}{k} = \frac{1}{T} \left[(C_1 - 1) \rho\varphi + C_2 \varphi \frac{P}{\epsilon} - C_3 \frac{P}{\epsilon} \right] \quad (17)$$

$\frac{\hat{P}_{22}}{k}$ will be discussed subsequently.

The modified pressure-strain term in Eqn. 16 is controlled by a wall-blocking function,

$$\beta = \beta(Re_T) \quad \beta \in [0, 1] \quad (18)$$

The limiting cases, $\beta = 0$ and $\beta = 1$, for the self-similar mean flow profile in a zero-pressure-gradient flat-plate are presented in Fig. 4. When $\beta = 0$, the anisotropy model produces essentially laminar flow ($\varphi \approx \frac{2}{3}$) through the shear layer. With $\beta = 1$, the model quickly forces a quasi-homogeneous shear flow, leading to a logarithmic velocity profile through the boundary layer. Clearly, a method of blending the two behaviors in the buffer between viscous and log layers is required.

Durbin[11] uses scalar elliptic relaxation to achieve this blending in the original v^2 - f model.

In the original notation of [28], the current coefficients map as $C_1 \mapsto C_1$, $C_2 \mapsto C_1^$, and $C_3 \mapsto (C_4/3 - C_5)$, and all values are reduced by a factor of two following the respective conventions for the anisotropy tensor definition. The current work uses the original SSG coefficients, which leads to C_3 being negligible.

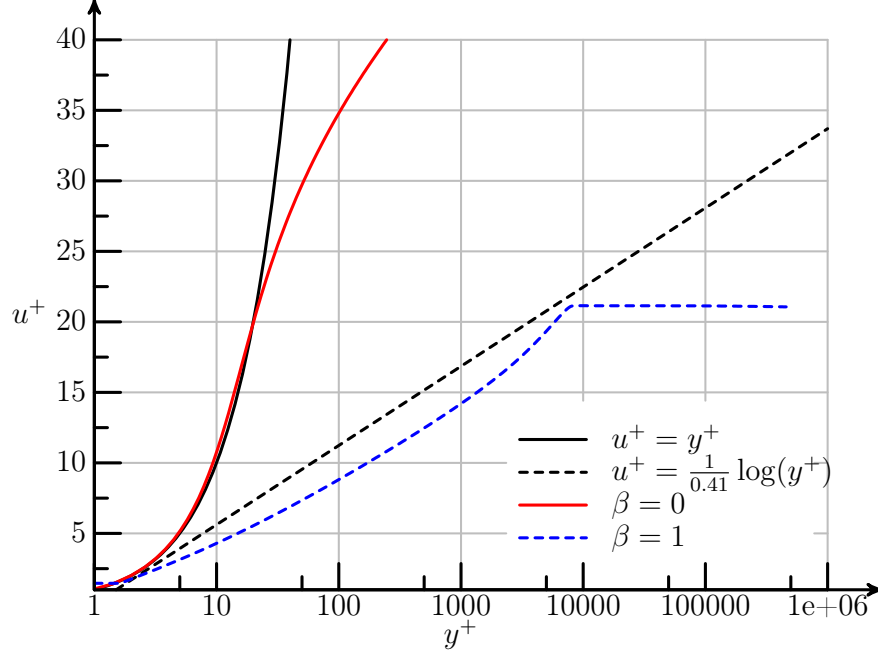


Figure 4: Mean flow velocity profile in zero-pressure-gradient flat-plate for limiting cases of pressure-blocking function. The offset from the classical log-layer profile is removed to emphasize the rapid transition through the viscous and buffer layers in the simulation.

In the current approach this would be

$$f - L^2 \partial_j [f_{,j}] = \hat{\Phi}_{22} \quad f \in [-\infty, \infty] \quad (19)$$

$$L = C_L \max \left[\frac{k^{3/2}}{\epsilon}, C_\eta \left(\frac{\nu^3}{\epsilon} \right)^{1/4} \right] \quad (20)$$

where C_L and C_η are calibration parameters, and f being substituted for $\beta \hat{\Phi}_{22}$ in Eqn. 16. A Dirichlet boundary condition on f is formulated to force $v_{,n}^2|_w = 0$, where n is the wall normal direction. In the current formulation, Eqn. 11 and the behavior of Eqn. 16 near the wall with $\beta = 0$ provide the appropriate behavior in the viscous layer, removing the need for an auxiliary boundary condition. In homogeneous shear regions the anisotropy is nearly constant and Eqn. 19 leads to

$$f \approx \text{const.} \quad \hat{\Phi}_{22} \approx \text{const.} \quad \partial_j [f_{,j}] \rightarrow 0 \quad L \rightarrow \infty \quad (21)$$

The v^2 - f formulations in the literature demonstrate sensitivity of the length scale coefficients to different flows and model formulations. Alternatively, Eqn. 19 is linearized to explicitly

provide an elliptic blending (*cf.* [22, 29]), however, this does not fundamentally change the sensitivity*.

Given these issues, and the associated numerical difficulties implementing the elliptic relaxation, here the appearance of physical justification is abandoned and the desired behavior of β is modeled directly using

$$\beta = \frac{1}{2} \left[1 + \tanh \left(\frac{5(Re_T - Re_T^*)}{Re_T^*} \right) \right] \quad (22)$$

with Re_T^* a calibration parameter and the behavior blending smoothly over a region $8Re_T^*/5$ (*cf.* Fig. 5). Re_T^* is determined by matching the extent of the buffer region in the experimental velocity profile for a zero-pressure-gradient flat plate at high Reynolds number, much as C_η is used to calibrate the v^2 - f model. In this manner, Re_T is used as a surrogate for the distance from the solid boundary in the current model. The pressure-strain model senses the presence of a wall (or other turbulent production mechanism) through the increase in local turbulent Reynolds number in the k - ϵ equations. This *ad-hoc* formulation performs well for self-similar wall-bounded flows across three orders of magnitude variation of Reynolds number. While the functional form of Eqn. 22 and the elliptic relaxation are different, there exist significant differences between the current formulation and the v^2 - f model, and hence there is no expectation that the blocking terms be identical. Numerically, the stiffness of the elliptic relaxation equation near the wall is avoided in the current approach, and tailoring numerical methods to include an elliptic modeling equation with a mixed hyperbolic-parabolic system is unnecessary. Further, the behavior in complex 3D flows containing multiple shear layers (separation, plumes) in general orientations is straightforward. Directly modeling β also provides a convenient mechanism to incorporate transition prediction and rough wall models into the eddy-viscosity model, though these topics are outside the scope of the current work.

The final term in Eqn. 16 to model is the production of velocity fluctuations normal to the shear layer, \hat{P}_{22} . In many flows this term is negligible, and it is normally not considered in v^2 - f models, however it is appreciable near separation and impingement regions. Modeling a single component of a tensor poses a difficulty, as we prefer the model is independent of orientation. Given that

$$\frac{P_{ij}}{k} = -a_{ik}u_{j,k} - a_{jk}u_{i,k} - \frac{4}{3}S_{ij} \quad (23)$$

*The homogenous form of the elliptic blending reduces to the scalar structure-based model proposed by Langer and Reynolds[30]. Benton[31] treats the elliptic blending and structure-based model variables interchangeably.

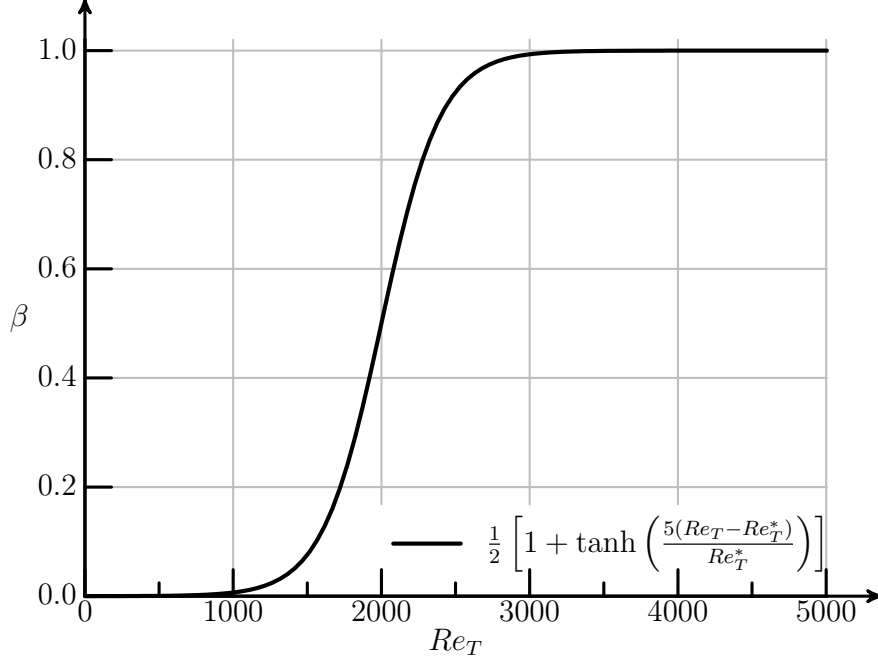


Figure 5: Wall-blocking blending function.

we choose

$$\frac{\hat{P}_{22}}{k} = \begin{cases} 2 \left(\frac{2}{3} - \varphi \right) [\partial_j (u_j \hat{n}_j)] \hat{n}_j & |\varphi_{,j}| \neq 0 \\ 0 & |\varphi_{,j}| = 0 \end{cases} \quad \hat{n}_j = -\frac{\varphi_{,j}}{|\varphi_{,j}|} \quad (24)$$

This approximation is independent of orientation, while still providing the necessary accounting in regions where the gradient of the wall-normal velocity in the direction normal to the shear layer is non-negligible. This will be investigated further in the numerical results of Sec. 3.3.

The coefficient of eddy-viscosity, C_μ , is chosen as follows. In a fully-developed homogeneous shear flow, Eqn. 16 reduces to

$$\left(\frac{2}{3} - \varphi \right) \frac{P}{\epsilon} - (C_1 - 1) \varphi - (C_2 \varphi + C_3) \frac{P}{\epsilon} = 0 \quad (25)$$

This leads to a constant value of anisotropy in regions where the ratio of production to dissipation rate is a constant, which is a good approximation for the log-layer. Using a typical value of $P/\epsilon \approx 1.5$ gives,

$$\varphi_h = \frac{(2 + 3C_3) \frac{P}{\epsilon}}{3 \left[C_1 - 1 + (C_2 + 1) \frac{P}{\epsilon} \right]} \approx 0.28 \quad (26)$$

Using this homogeneous value of the anisotropy, and following the same arguments which lead to C_μ for the original k - ϵ derivation ($-\langle u'_1 u'_2 \rangle \approx 0.3k$ in the log layer), gives $C_\mu = 0.11$. This same value is obtained to two significant digits for $P/\epsilon \in [0.9, 2.8]$ under this quasi-homogeneous assumption, so there is little sensitivity. Thus the eddy-viscosity coefficient is modified from the standard k - ϵ value, but is done so in a manner consistent with the original model development. As we will see in Sec. 3, the component of anisotropy normal to the shear layer in quasi-homogeneous regions is not a universal constant. Rather than choosing a specific situation to calibrate the pressure-strain coefficients, the original SSG model is retained. Improvements to the pressure-strain modeling that allow more complex behavior is left for future work.

While Eqn. 11 represents a scalar anisotropy approximation, it is still instructive to examine the full anisotropy tensor. By enforcing $a_{ii} = 0$ and assuming $\langle u'_3 u'_3 \rangle = 1/2 (\langle u'_1 u'_1 \rangle + \langle u'_2 u'_2 \rangle)$, the scalar anisotropy model is prolonged to a full tensor without introducing new model parameters. This gives

$$a_{ij} = \begin{pmatrix} \varphi & a_{12} & a_{31} \\ a_{12} & -\varphi & a_{23} \\ a_{31} & a_{23} & 0 \end{pmatrix} \quad (27)$$

where the off-diagonal components are given by $a_{ij} \simeq C_\mu \left[1 - \left(\frac{3}{2}\varphi \right)^2 \right] T u_{i,j}$. Varying the Reynolds stress components and anisotropy we can construct contours within Lumley's triangle (cf. Fig. 6). The model symmetrically elongates the energy distribution, and collapses to the $\xi_{III} = 0$ line for planar shear. As designed, the model restricts to isotropic and pure two-component flow for the limiting values of the scalar anisotropy, $\varphi = 0$ and $|\varphi| = 2/3$ respectively.

2.1 Numerical Implementation

The complete set of eddy-viscosity model equations is given in by

$$\frac{d}{dt} \int \hat{q}_l d\Omega + \oint (\hat{f}_{lj} - \hat{g}_{lj}) n_j d\Gamma = \int \hat{h}_l d\Omega \quad (28)$$

$$\hat{q}_l = \begin{pmatrix} \rho k \\ \rho \epsilon \\ \rho \varphi \end{pmatrix}, \quad \hat{f}_{lj} n_j = \begin{pmatrix} \rho k u_n \\ \rho \epsilon u_n \\ \rho \varphi u_n \end{pmatrix},$$

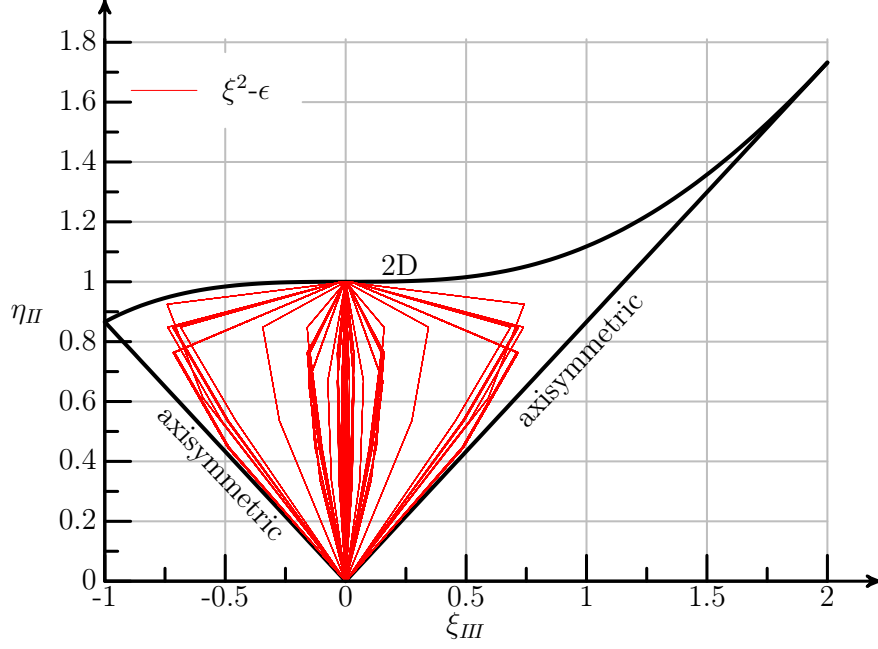


Figure 6: Lumley triangle of scaled invariants of the Reynolds-stress anisotropy tensor

$$\hat{g}_{lj} = Re_{\text{ref}}^{-1} \left\{ \begin{array}{l} \left(\mu + \frac{\mu_t}{\sigma_k} \right) k_{,j} \\ \left(\mu + \frac{\mu_t}{\sigma_\epsilon} \right) \epsilon_{,j} \\ \left(\mu + \frac{\mu_t}{\sigma_\varphi} \right) \varphi_{,j} \end{array} \right\} \quad (29)$$

$$\hat{h}_l = \left\{ \begin{array}{l} P - \hat{D} \\ \frac{C_{\epsilon_1} P - C_{\epsilon_2} \hat{D}}{T} \\ \frac{1}{T} \left[\left(\frac{2}{3} - \varphi \right) \left(\frac{P}{\epsilon} + \frac{\hat{P}_{22}}{\epsilon} \right) - \beta \frac{\hat{\Phi}_{22}}{\epsilon} \right] \end{array} \right\} \quad (30)$$

with $P = \left[2 \frac{\mu_t}{Re_{\text{ref}}} \left(S_{ij} - \frac{1}{3} u_{k,k} \delta_{ij} \right) - \frac{2}{3} \rho k \delta_{ij} \right] S_{ij}$, and $\frac{\mu_t}{Re_{\text{ref}}} = C_\mu \rho \xi^2 T$. The model coefficients are provided in the Nomenclature section. The standard values of the coefficients for the k - ϵ and SSG models are used, with the aforementioned exception of C_μ . The turbulent dissipation is modified as

$$\hat{D} = \rho \epsilon - (\rho \epsilon)_\infty \quad (31)$$

to remove the non-physical dependence of the model on the numerical boundary conditions in the far field.

The minimum and maximum turbulent time scale is limited by the Kolmogorov timescale ($\sqrt{\frac{\nu}{\epsilon}}$) and Durbin's realizability constraint[32] ($\frac{k}{\sqrt{6} C_\mu \xi^2 S^*}$), respectively, where $S^* = \sqrt{S_{ij}^* S_{ij}^*}$ is the magnitude of the compressible strain-rate tensor. The realizability constraint is undefined

in strain-free flow, so the minimum specific dissipation rate $\omega_{min} = \sqrt{6}C_\mu \left[1 - \left(\frac{3}{2}\varphi\right)^2\right] S^*$, rather than maximum timescale is substituted. The limits are imposed using a smooth approximation to the maximum function,

$$\max_{C^\infty}(a, b) = \frac{1}{2} \left[a + b + \sqrt{(a - b)^2 + \delta^2} \right] \quad \delta \ll a, b \quad (32)$$

so that

$$\frac{1}{T} = \max_{C^\infty} \left(\frac{1}{\max_{C^\infty} \left(\frac{k}{\epsilon}, \sqrt{\frac{\nu}{\epsilon}} \right)}, \omega_{min} \right). \quad (33)$$

Eqns. 1 and 28 are combined and solved as a monolithic coupled system using a standard 2nd-order finite-volume scheme. The inviscid flux vector is upwinded using Roe's approximate Riemann solver[33] and the Koren slope limiter[34], while the viscous and source terms are evaluated using centered formulas.

At a solid boundary, no-slip and adiabatic wall are specified for the mean flow equations. For the turbulence variables, we have

$$k|_w = k_{,n}|_w = 0 \quad \varphi|_w = \frac{2}{3} \quad (34)$$

We also have

$$u_n \rightarrow 0 \quad \mu'_t \rightarrow 0 \quad P \rightarrow 0 \quad (35)$$

at a smooth, impermeable wall, so that the transport of turbulent kinetic energy reduces to,

$$\epsilon|_w = \partial_{,n}(\nu k_{,n})|_w \quad (36)$$

Integrating this expression near the wall gives,

$$\epsilon|_w y = \nu k_{,n}|_y - \nu k_{,n}|_w \quad \Rightarrow \quad \epsilon|_w = \frac{\nu k_{,n}|_y}{y} \quad (37)$$

where y is the distance normal to the wall. This provides a Dirichlet boundary condition on the dissipation which is evaluated in a manner consistent with the numerical approximation, *e.g.* using higher-order approximations for the wall-normal gradient if appropriate. Note that the common practice, $\epsilon|_w = \frac{2\nu k|_y}{y^2}$, provides a first-order approximation to Eqn. 37.

For external flow simulations, the farfield values of the turbulence quantities are specified

as

$$k|_{\infty} = \frac{3}{2}Tu^2u_{\infty}^2, \quad Re_T|_{\infty} = 1, \quad \varphi|_{\infty} = 0 \quad (38)$$

where Tu is the turbulence intensity, and $u_{\infty}^2 = u_i u_i|_{\infty}$.

To enhance stability, \hat{h}_l is split into source and off-diagonal sink contributions (\hat{h}_l^+) and the diagonal sink contributions (\hat{h}_l^-). \hat{h}_l^+ is treated explicitly and \hat{h}_l^- implicitly. Commonly, the dissipation in the k equation ($-\rho\epsilon$) is transformed to improve the diagonal dominance of the implicit scheme[35], however this increases the stiffness of the equation set, as ϵ becomes large as the wall is approached. The decomposition of the eddy viscosity (Eqn. 11) provides an alternative. The turbulent kinetic energy production term is split into the difference of an isotropic (P^i) and anisotropic (P^a) contribution,

$$P = \left[2\mu_t \left(S_{ij} - \frac{1}{3}u_{k,k}\delta_{ij} \right) - \frac{2}{3}\rho k\delta_{ij} \right] S_{ij} \quad (39)$$

$$= 2\mu_t \left[S^2 - \frac{1}{3}(u_{k,k})^2 \right] - \frac{2}{3}\rho k u_{k,k} \quad (40)$$

$$= 2C_{\mu}\rho k T S_c^2 - 2C_{\mu}^*\rho k \varphi T S_c^2 - \frac{2}{3}\rho k u_{k,k} \quad (41)$$

$$= P^i - P^a \quad (42)$$

where $S_c^2 = S^2 - \frac{1}{3}(u_{k,k})^2$, and

$$P^i = 2C_{\mu}\rho k T S_c^2 \quad (43)$$

$$P^a = 2C_{\mu}^*\rho k \varphi T S_c^2 + \frac{2}{3}\rho k |u_{k,k}| \quad (44)$$

Selectively linearizing the appropriate contribution of the production improves the diagonal dominance of implicit schemes in wall-bounded regions without unnecessarily increasing the stiffness of the system.

The diagonal sink term is

$$\hat{h}_l^- = \left\{ \begin{array}{c} 0 \\ 0 \\ 0 \\ -P^a \\ \frac{-C_{\epsilon_2}\rho\epsilon}{T} \\ -\frac{1}{T} \left[\frac{2}{3}\frac{P^a}{\epsilon} + \varphi\frac{P^i}{\epsilon} + C_1\rho\varphi + C_2\varphi\frac{P^i}{\epsilon} \right] \end{array} \right\} \quad (45)$$

The mean flow and turbulent quantities are considered decoupled in linearizing \hat{h}_l^- .

3 Numerical Results

Numerical simulations using the turbulence model described in the previous section are compared against standard implementations of the SA and SST models and benchmark experimental data. The SA and SST model simulations are computed with the OVERFLOW solver[36] using the Roe upwind scheme with Koren limiter to match the current model implementation. A mesh resolution study was computed for all numerical experiments and for each turbulence model individually. Little difference in mesh sensitivity is noted between the models, and the presented results were computed using the same finest mesh for all models. The experimental data for the presented cases is at low speed, where incompressible flow is typically assumed. The current work uses a low Mach number ($M_\infty = 0.15$), and assumes the compressibility effects are negligible relative to the modeling errors.

3.1 Zero-Pressure-Gradient Flat Plate

The computed results for a high-Reynolds-number zero-pressure-gradient flat-plate boundary layer are compared against the experimental data of DeGraaff and Eaton[37] in Fig. 7. As expected, all models provide good predictions of the mean flow velocity profile, as all were calibrated for this specific flow. The current model does provide an improvement in the outer portions of the log layer and wake region of the velocity profile. Both SA and SST overpredict the extent of the boundary layer at this Reynolds number.

It is interesting to compare the different modeling approaches for this case. SA models the turbulent eddy viscosity directly to provide the desired Reynolds stress profile. As this is a planar self-similar flow, the Reynolds shear stress and mean velocity are directly coupled, and this approach provides good agreement in the mean flow. The SST model uses a similar approach, however based on the transport equations for the turbulent kinetic energy and specific dissipation rate. As seen, the turbulent kinetic energy in the near-wall region is not intended as a physical prediction using the SST model, but rather to provide the correct Reynolds stress behavior in combination with the modeled ω variation. In the current approach, the intent is to model the actual profiles of the turbulent fluctuations through the boundary layer. It is felt that this approach will provide improvements in predictions for more complex cases outside the model calibration. The predictions of turbulent kinetic energy and scalar anisotropy profiles using the current model are in good qualitative agreement with

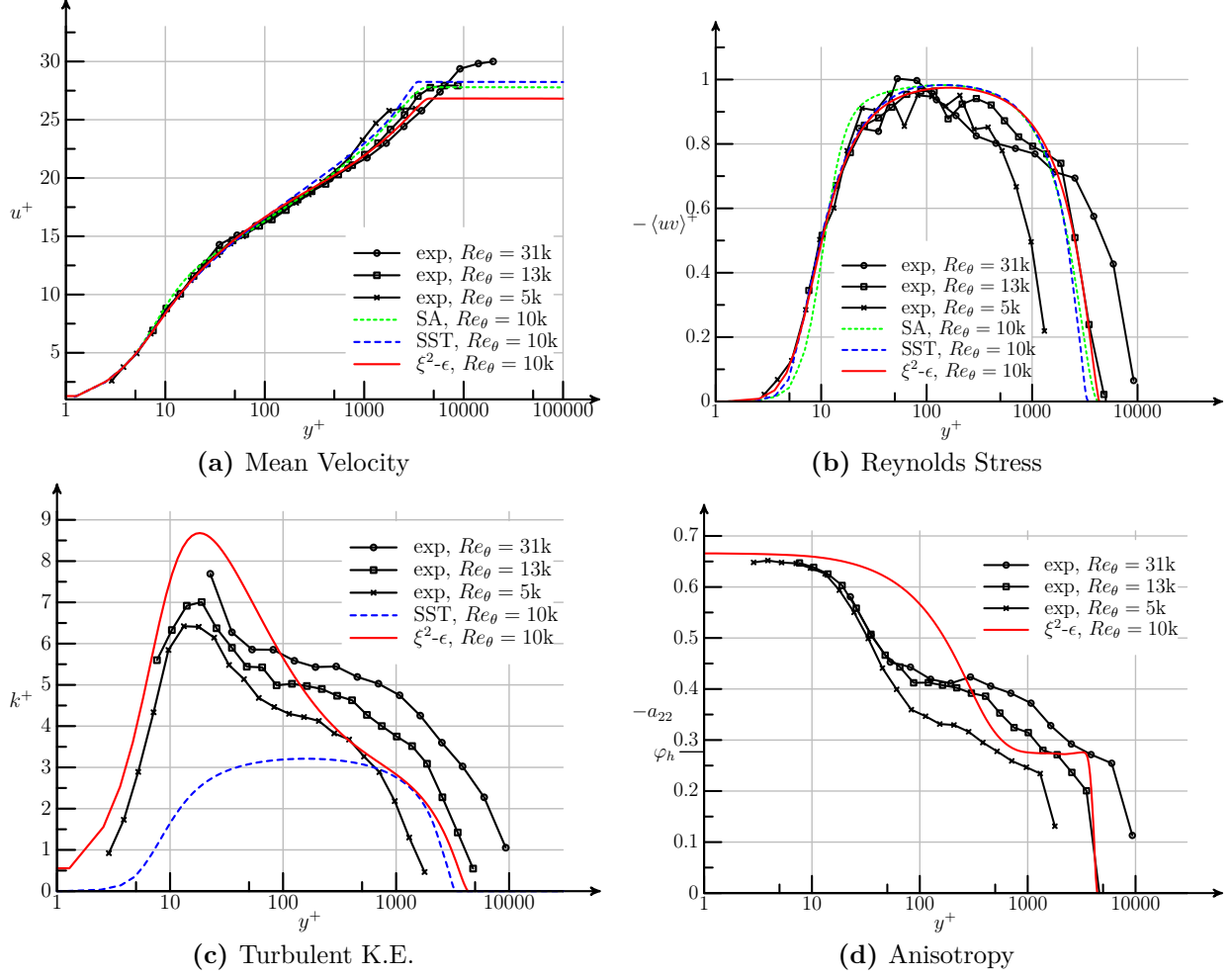


Figure 7: Computed results for the zero-pressure-gradient flat plate. Experimental data from DeGraaff and Eaton[37].

the experimental variation*. The current model overpredicts the turbulent kinetic energy in the buffer layer. The anisotropy does not decay quickly enough through the buffer layer, and in the log layer the homogeneous value of the anisotropy predicted by the SSG model is not in good agreement with the measured value for this wall-bounded flow.

3.2 Planar Mixing Layer

A planar mixing layer is computed in a fixed inertial frame until a self-similar state is reached. The computed spreading rate for simulations with the three different turbulence

*The scalar anisotropy in the current model is intended to reduce to $-a_{22}$ in planar flow, and hence the modeled anisotropy is presented directly against the physical measurements.

	Spreading Rate
Exp.	0.06–0.11
SA	0.065
SST	0.069
ξ^2 - ϵ	0.063

Table 1: Mixing-layer spreading rate, $\frac{u_c}{u_s} \frac{d\delta}{dx}$, where u_c and u_s are the average and difference respectively of the velocity of the parallel streams.

models is presented in Table 1, and the self-similar profiles are compared against the experimental data of Bell and Mehta[38] in Fig. 8. All three models predict a spreading rate towards the low end of the experimental range. The SA model is again calibrated directly for this flow, and the predicted results for Reynolds stress and mean velocity are in good agreement with the measured data. The SST model underpredicts the turbulent diffusion at the edges of the shear layer. As noted in [39], this deficiency is straightforward to correct, however the standard model coefficients are maintained here for a baseline comparison. The current model predicts good agreement with the measured mean velocity, and the accuracy of the model is consistent with predictions of the standard (isotropic) k - ϵ model in the literature for this free shear layer, which is the design intent. The variation of turbulent kinetic energy is underpredicted, however this may be due to the known sensitivity of this flow to initial conditions. Here the homogeneous value of the scalar anisotropy slightly overpredicts the experimental measured value, though again the qualitative features are well predicted.

3.3 Periodic Hills

The final computational case is the planar flow over periodically arranged hills[40]. This flow is challenging, due to the coupling between the smooth-body separation location and the recirculation region (*cf.* Fig. 9), however computationally amenable given the streamwise periodic flow. Unlike the previous numerical experiments, in this situation none of the models has been calibrated for this flow archetype, and hence this is a representative predictive test for separated flows.

The non-periodic pressure gradient is applied using a streamwise momentum source,

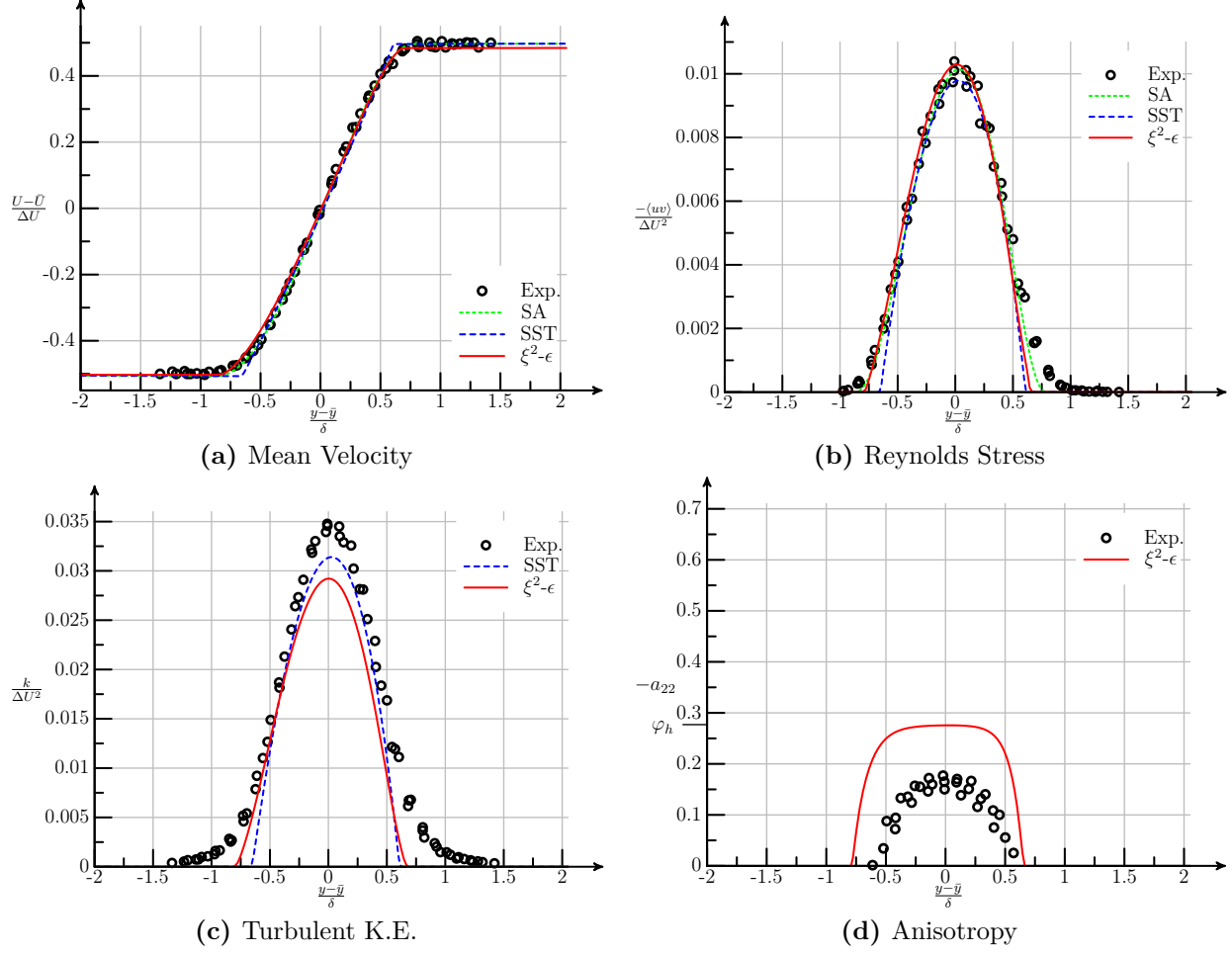


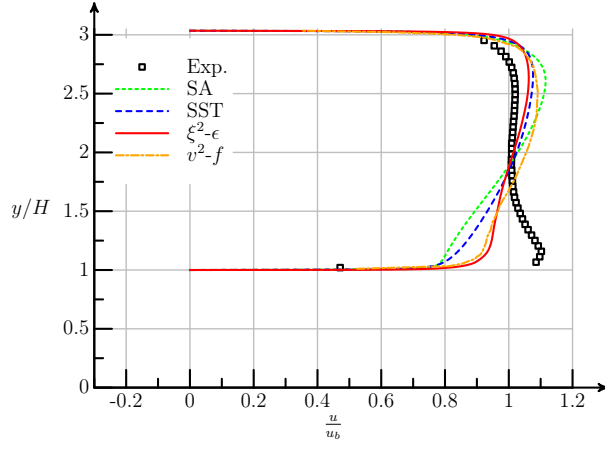
Figure 8: Computed results for the planar mixing layer. Experimental data from Bell and Mehta[38].

similar to the approach used by Huang *et al.* for compressible channel flow simulations[41]

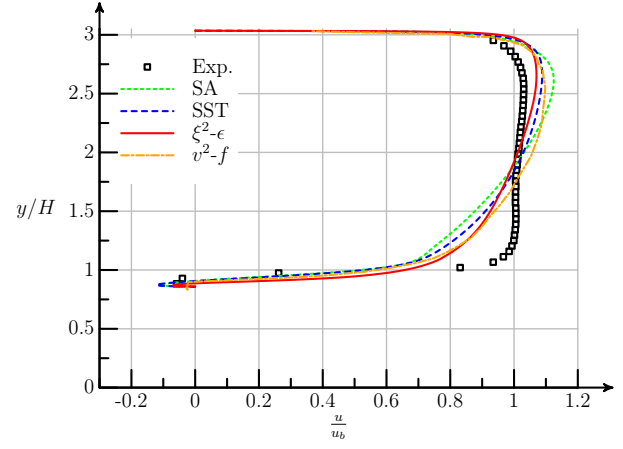
$$h_l = \left\{ \begin{array}{c} 0 \\ \frac{\hat{d}p}{dx} \frac{\rho}{\rho_b} \\ 0 \\ 0 \\ u_1 \frac{\hat{d}p}{dx} \frac{\rho}{\rho_b} \end{array} \right\} \quad (46)$$

where here $\frac{\hat{d}p}{dx}$ is adjusted until the desired bulk Reynolds number over the peak of the hill, $Re_b = \frac{u_b H}{\nu_b}$, is achieved. A similar approach using a time-varying source term was successfully applied to large-eddy simulations for the same configuration[42].

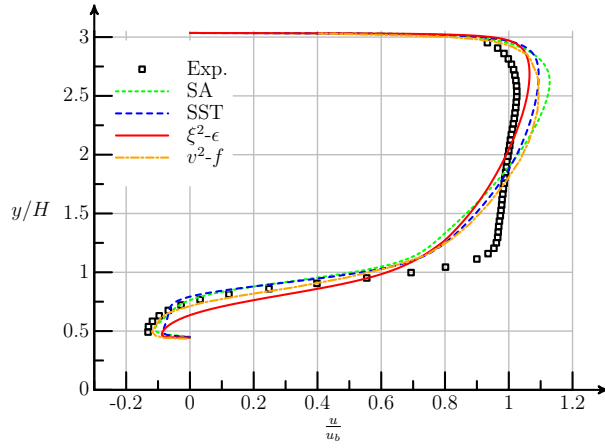
The experimental particle image velocimetry (PIV) data does not contain sufficient



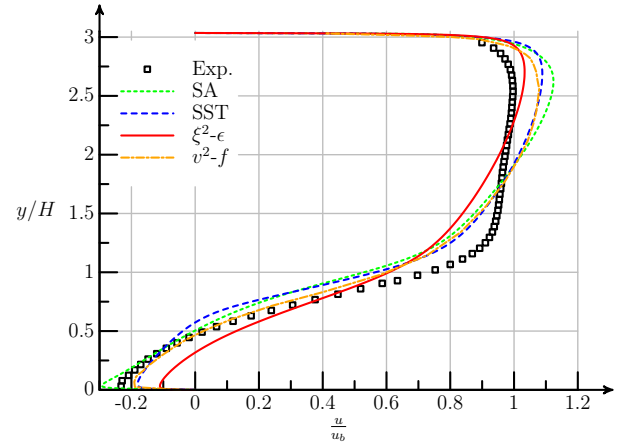
(a) $x/H = 0.05$



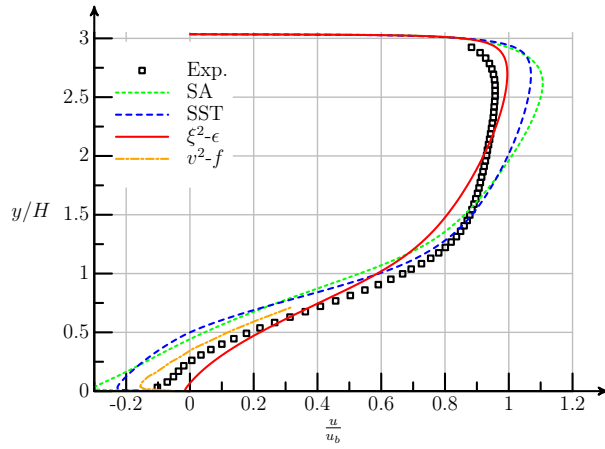
(b) $x/H = 0.5$



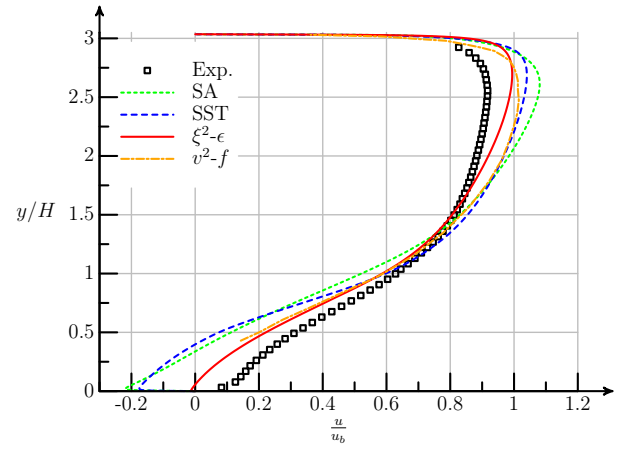
(c) $x/H = 0.1$



(d) $x/H = 0.2$



(e) $x/H = 0.3$



(f) $x/H = 0.4$

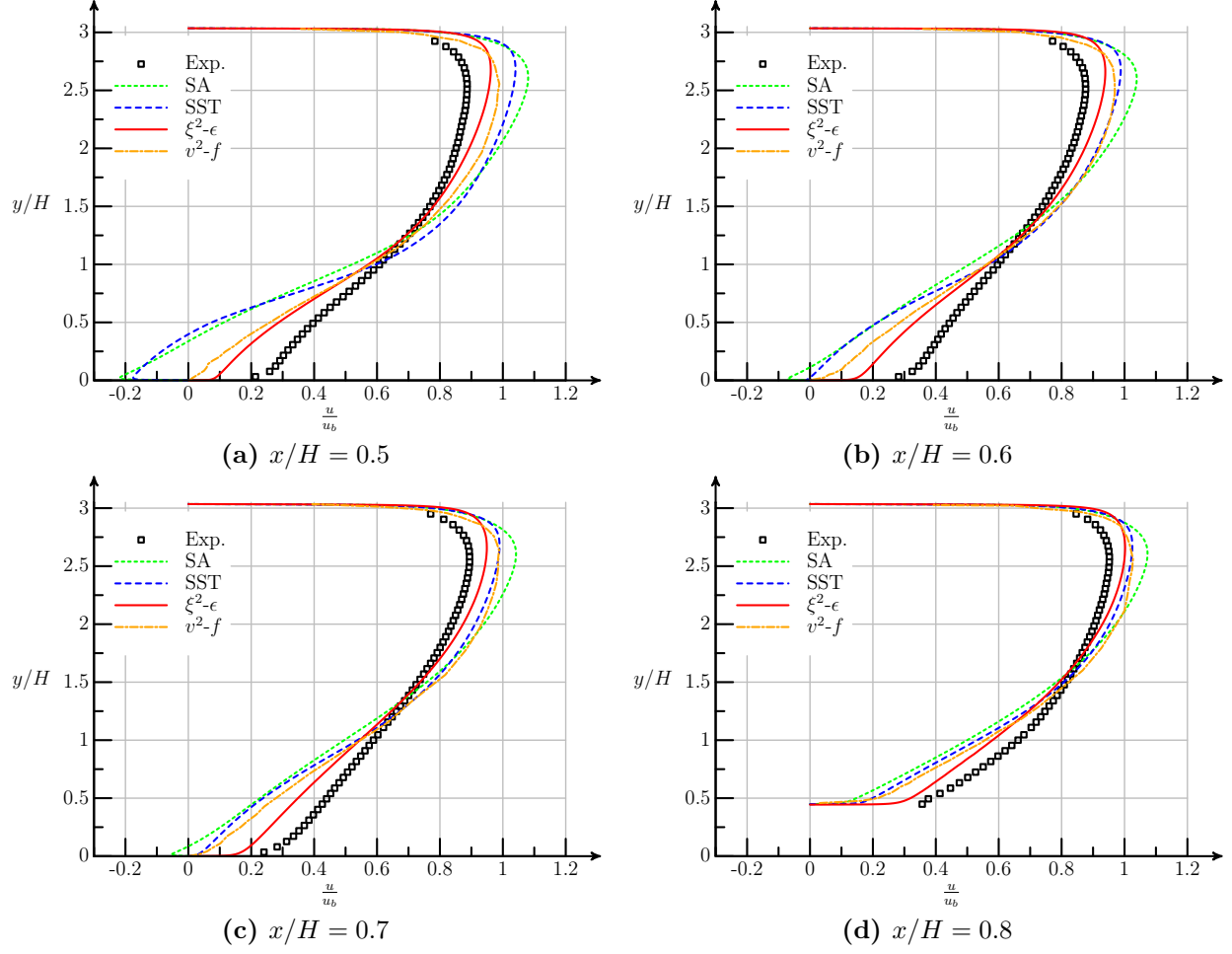
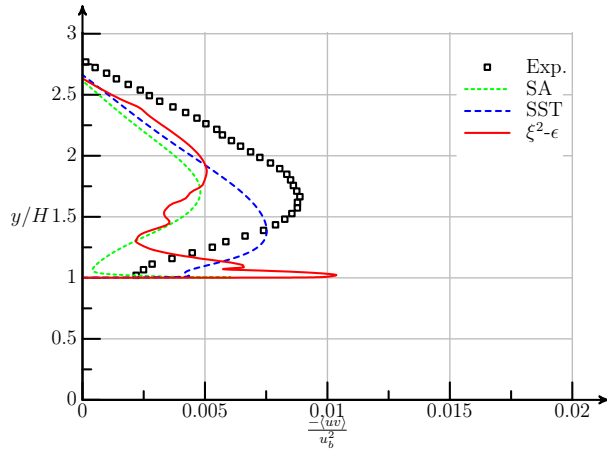
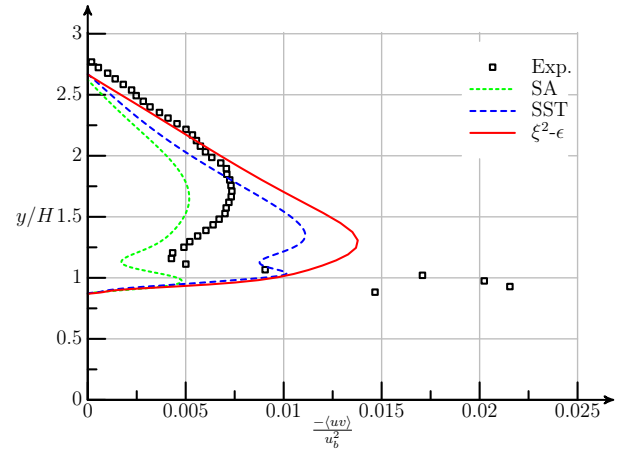


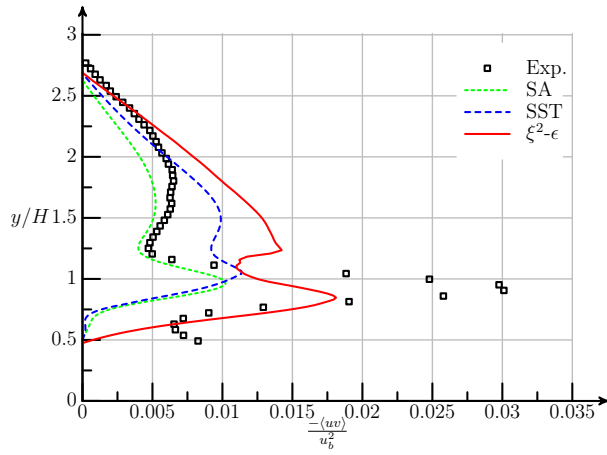
Figure 10: Computed mean velocity for the periodic hills. v^2-f simulation results from Billard and Laurence[22]. Experimental data from Rapp and Manhart[40] at $Re_b = 39k$.



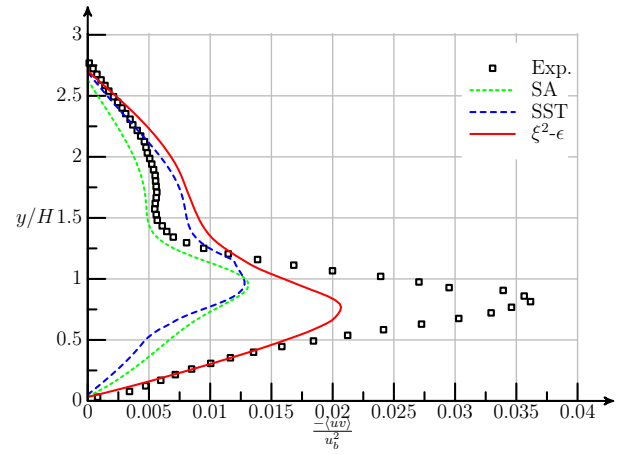
(a) $x/H = 0.05$



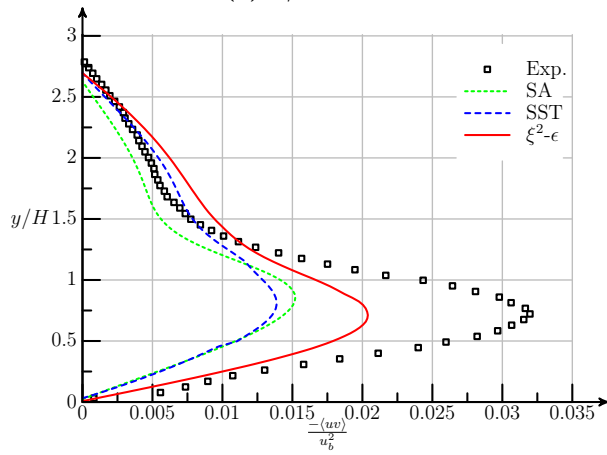
(b) $x/H = 0.5$



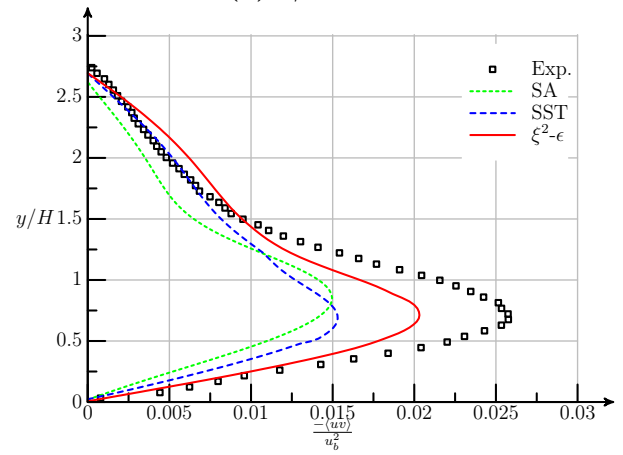
(c) $x/H = 0.1$



(d) $x/H = 0.2$



(e) $x/H = 0.3$



(f) $x/H = 0.4$

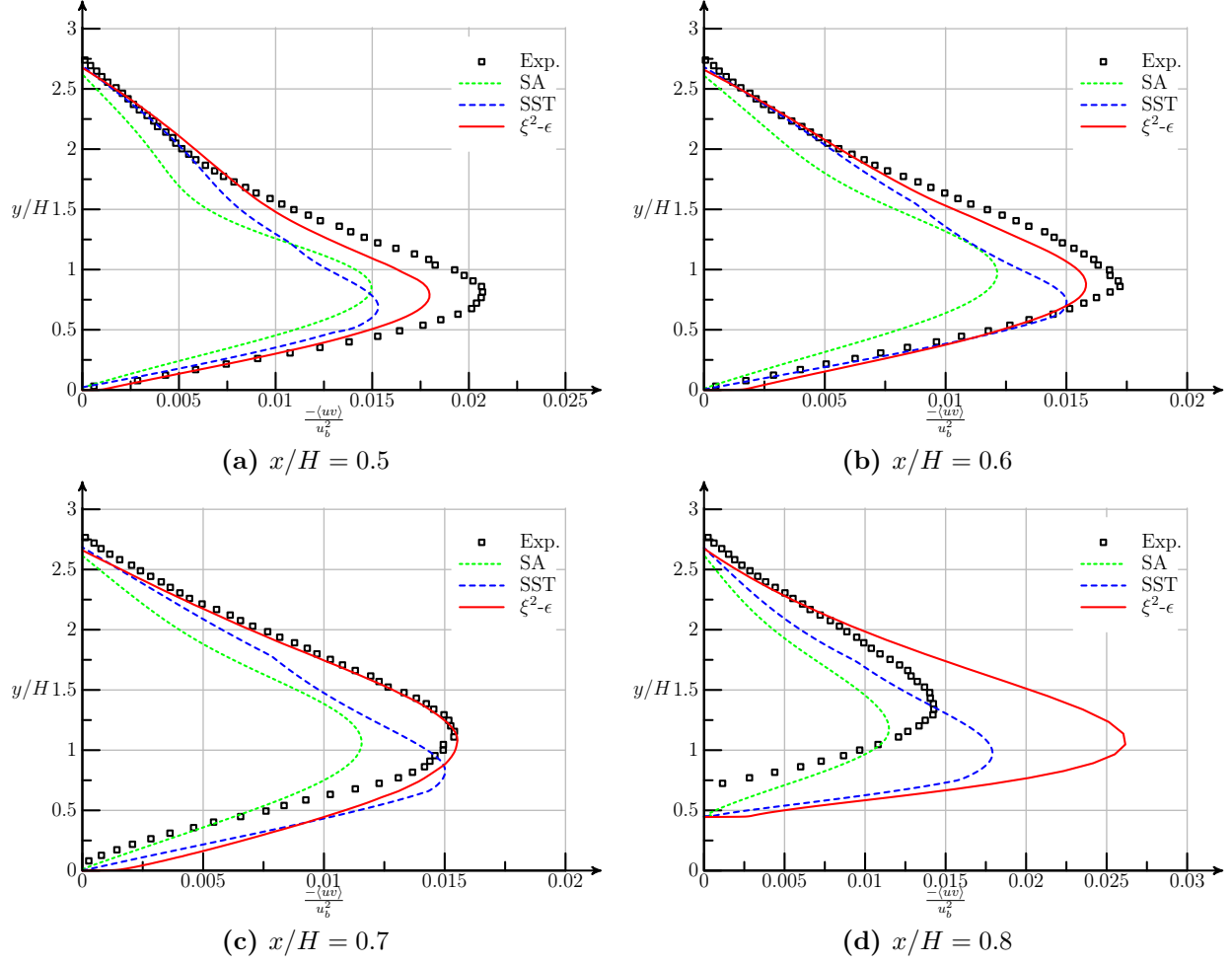
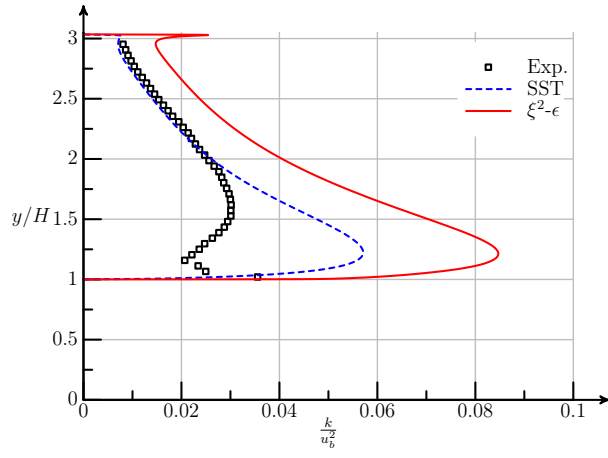
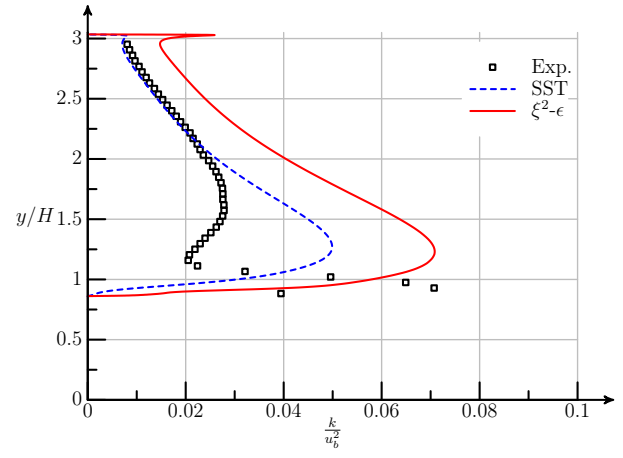


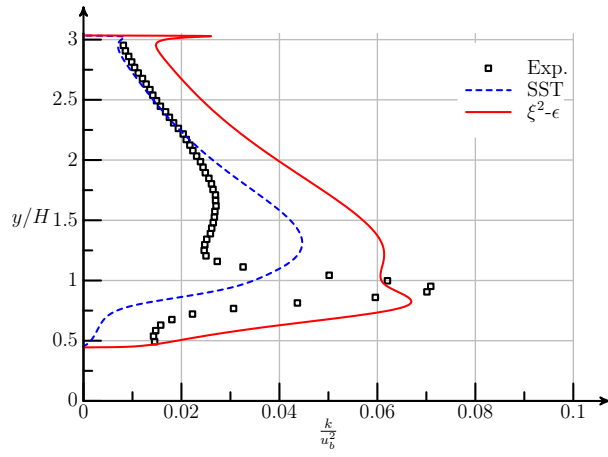
Figure 11: Computed planar Reynolds stress for the periodic hills. Experimental data from Rapp and Manhart[40] at $Re_b = 39k$.



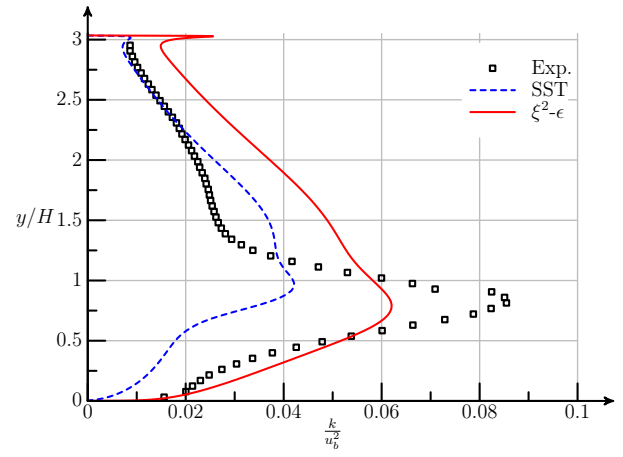
(a) $x/H = 0.05$



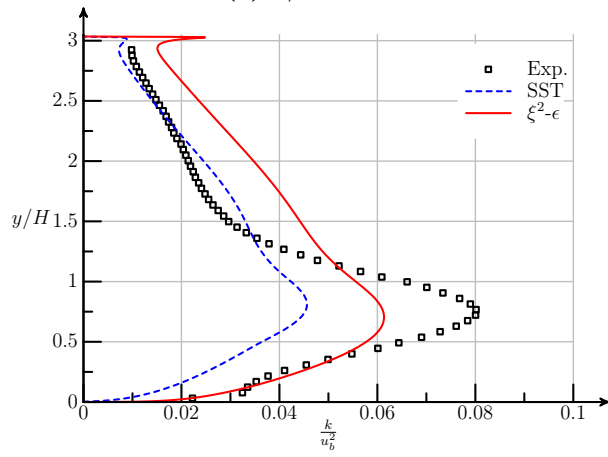
(b) $x/H = 0.5$



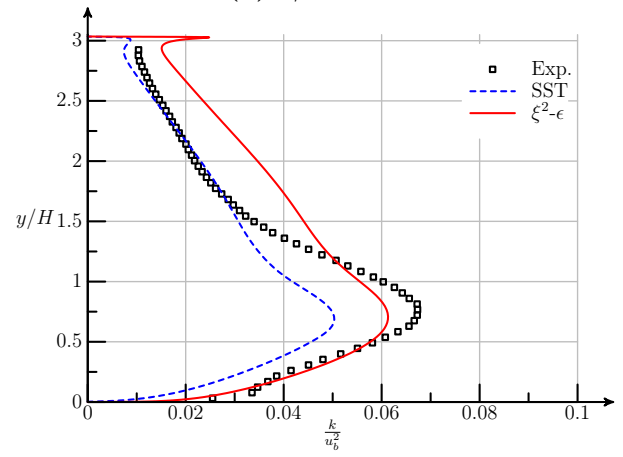
(c) $x/H = 0.1$



(d) $x/H = 0.2$



(e) $x/H = 0.3$



(f) $x/H = 0.4$

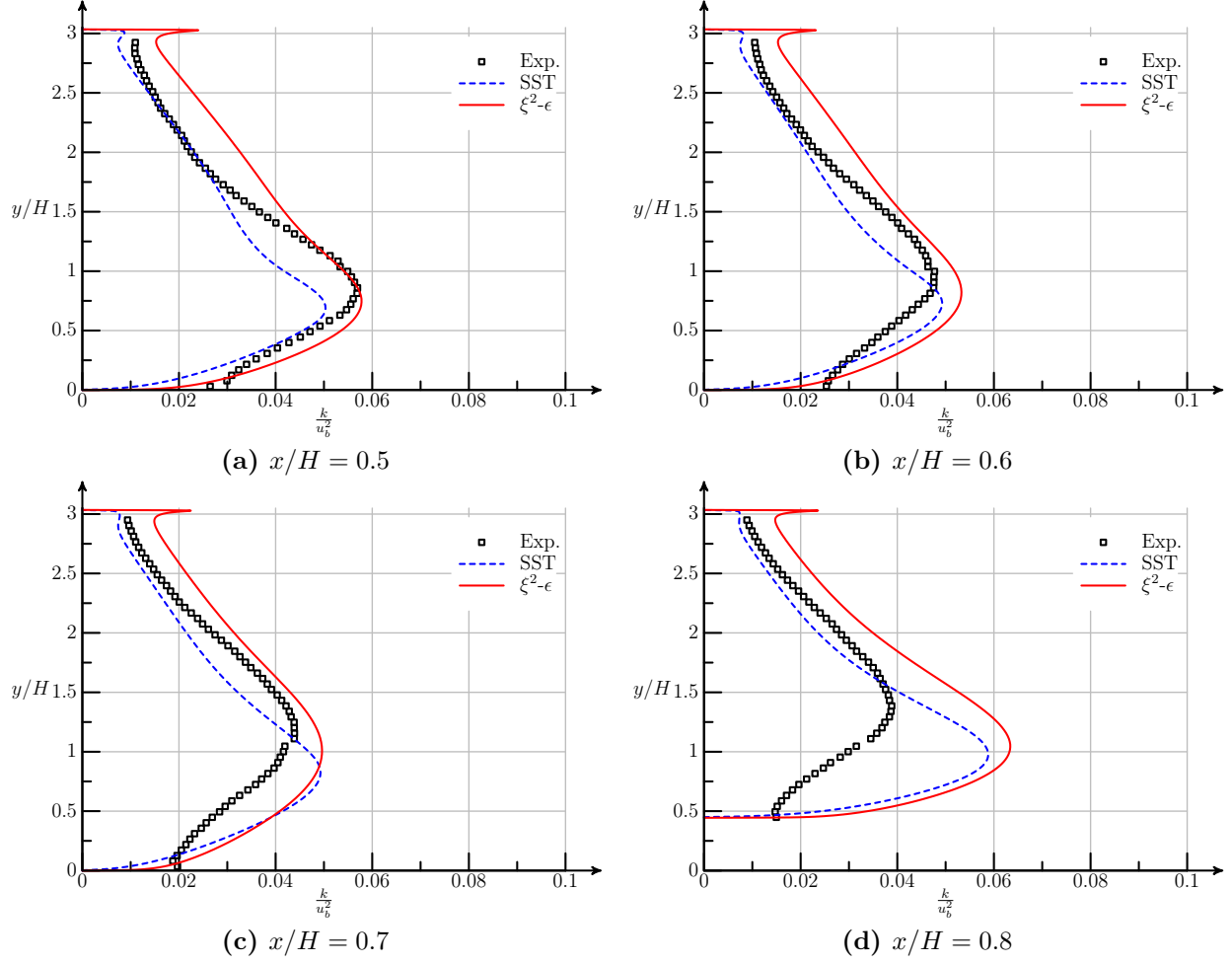
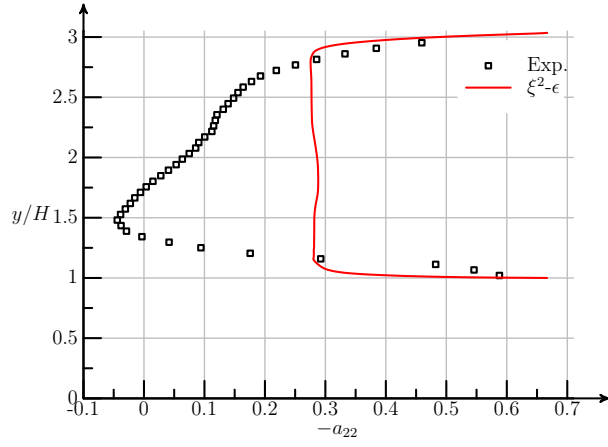
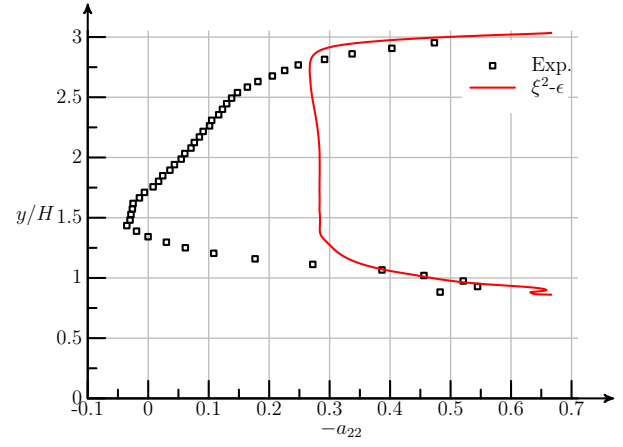


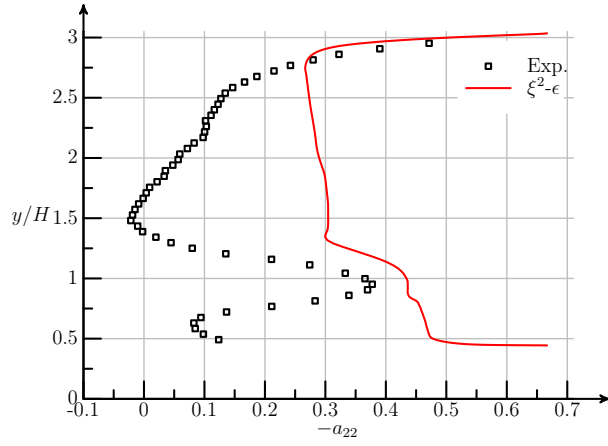
Figure 12: Computed turbulent kinetic energy for the periodic hills. Experimental data from Rapp and Manhart[40] at $Re_b = 39k$.



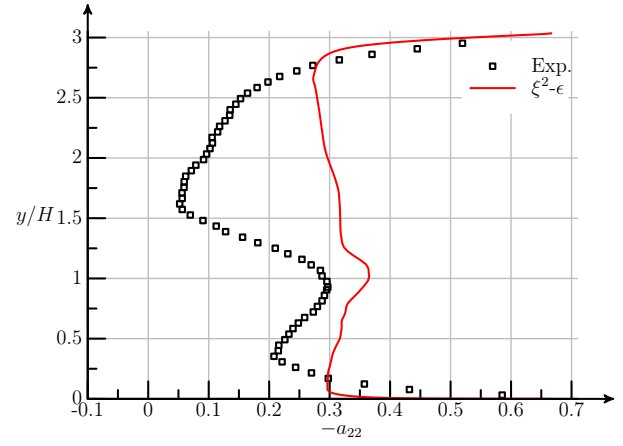
(a) $x/H = 0.05$



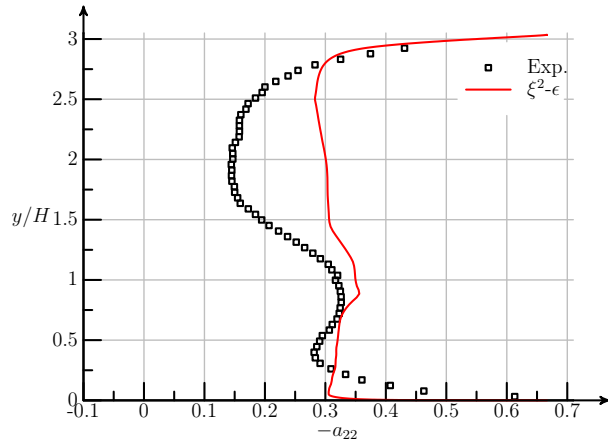
(b) $x/H = 0.5$



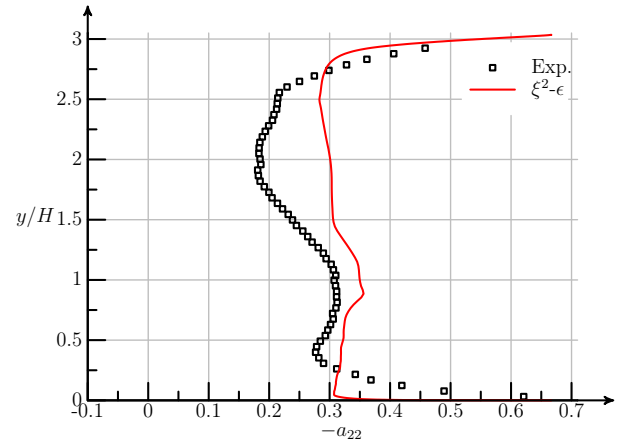
(c) $x/H = 0.1$



(d) $x/H = 0.2$



(e) $x/H = 0.3$



(f) $x/H = 0.4$

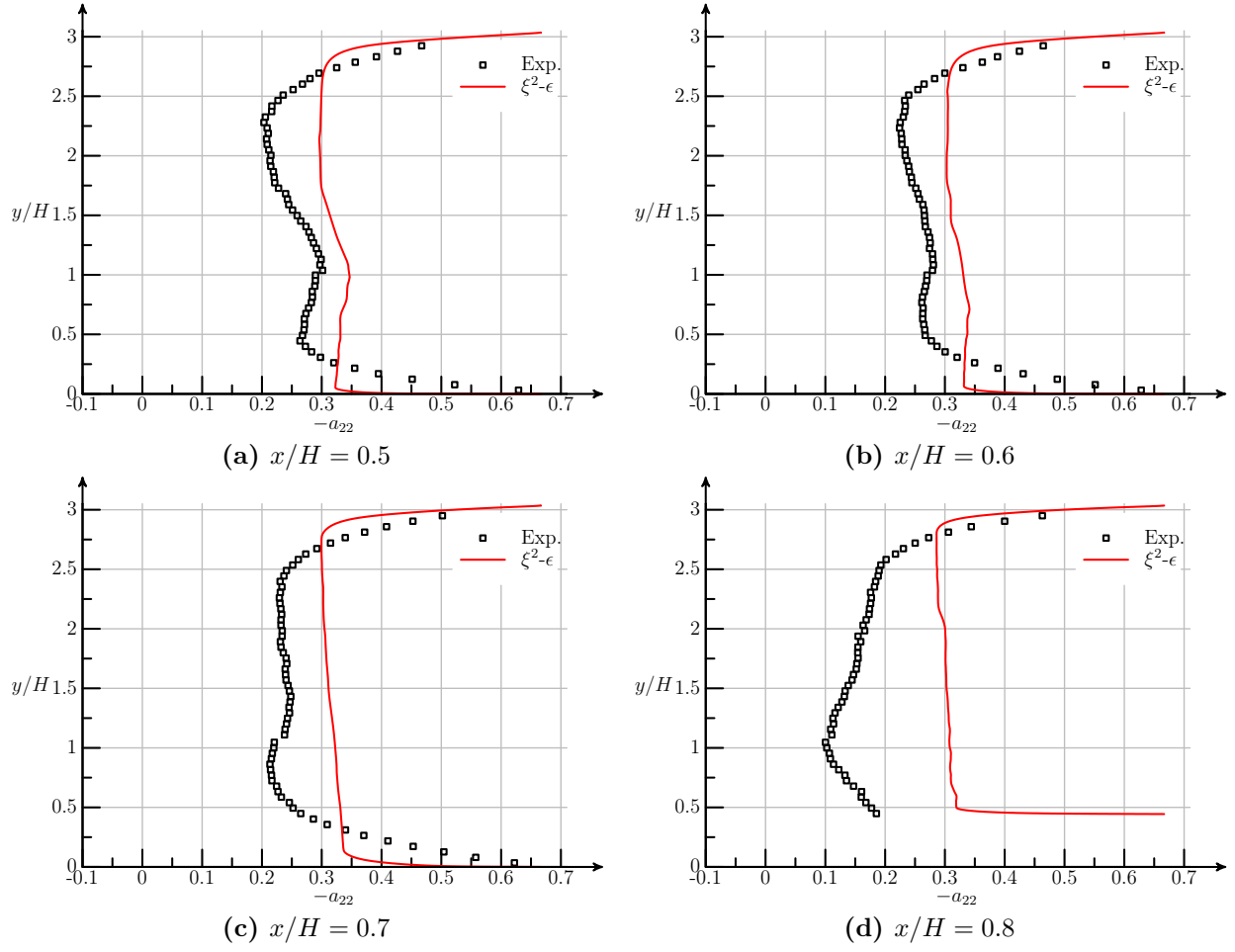


Figure 13: Computed anisotropy for the periodic hills. Experimental data from Rapp and Manhart[40] at $Re_b = 39k$.

resolution near the separation location at the peak of the hill to reliably reproduce streamlines in this region, however, the main recirculation region is clearly visible in Fig. 9. The current model slightly underpredicts the height and length of the recirculation region. The SA and SST models greatly exaggerate the extent of the recirculation zone, with the SA model predicting reversed flow along the entirety of the flat section between the hills.

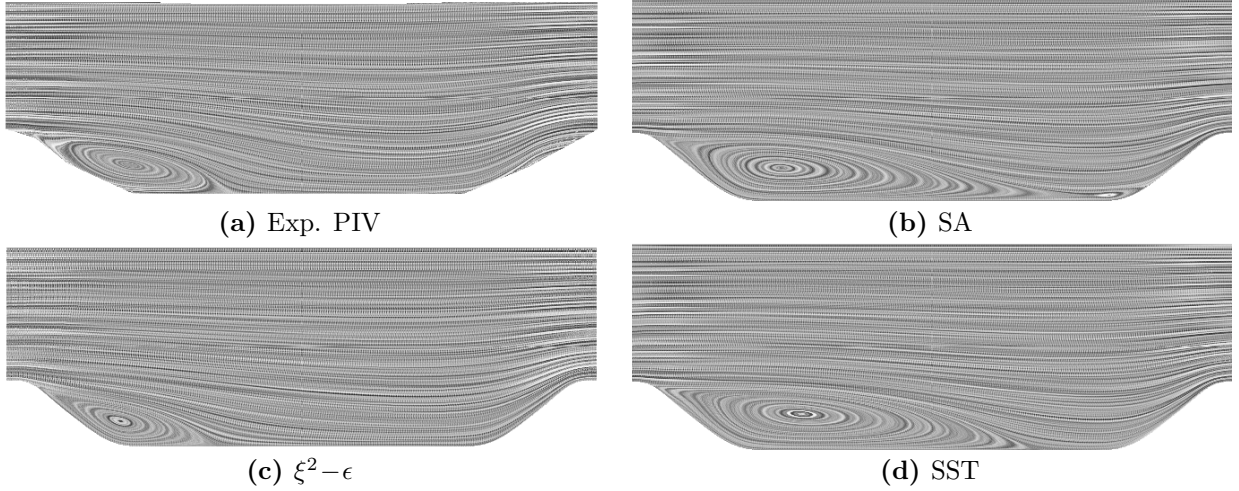


Figure 9: Streamlines visualized using line-integral convolution of the velocity vector[43]. Experimental data from Rapp and Manhart[40] at $Re_b = 39k$.

The quantitative PIV data is available at 10 streamwise stations, and the comparisons of mean flow and turbulence predictions against this data are presented in Figs. 10-13. The mean velocity profiles for a standard version of the v^2-f model from Billard and Laurence[22] are also included*. The current model in general provides an improved prediction relative to the baseline models, most notably in the recirculation region, though none of the models demonstrate good quantitative predictive capability in this case. The current model demonstrates a consistent improvement over the v^2-f model near the upper wall and downstream of the recirculation region. None of the models capture the mean flow velocity overshoot near the hill peak in the experimental data at $x/H = 0.05$. The current model is strongly overpredicting the production of turbulent kinetic energy in the favorable pressure gradient on the upstream portion of the hill, reminiscent of the discussion of the flat-plate predictions. Similarly, the anisotropy is again forced to the homogeneous value over much of the channel width, which is clearly at odds with the physical behavior, especially near the separation location. The approach of modeling the Reynolds-stress anisotropy using a single component

*The gaps in the profiles are in the original data.

of the tensor necessarily removes the coupling terms between components in the tensor, such as streamline curvature. This is sufficient in self-similar wall-bounded flows, where $\langle u'_1 u'_1 \rangle$ dominates and the anisotropy normal to the wall captures much of the behavior of the full tensor. In this separating flow, the behavior is more complex, and additional information is likely required to accurately characterize the main features of the Reynolds-stress tensor.

The modeled production of velocity fluctuations normal to the shear layer, $\frac{\hat{P}_{22}}{k}$ from Eqn. 24, is negligible in both the flat-plate and mixing-layer simulations. Contours of $\frac{\hat{P}_{22}}{k}$ relative to $\frac{P}{k}$ is presented in Fig. 14. In most regions of the flow domain the magnitude of $\frac{\hat{P}_{22}}{k}$ is negligible. The exceptions are the curvature of the attached flow upstream of the peak of the hill, and the region near the separation and in the separated shear layer itself, on the aft portion of the hill. While the magnitude is relatively small, this term allows the anisotropy to “recognize” the separated shear layer, and provides the increase in anisotropy near $y/H = 1$ in Fig. 13. When this term is removed, the extent of the recirculation region is reduced by roughly 25% and the correlation with the experimental data suffers.



Figure 14: Contours of \hat{P}_{22}/P in the range $[0, 0.07]$.

4 Summary

The current work presents a novel turbulence model in the spirit of Durbin’s v^2 - f model, which naturally recovers to a self-consistent isotropic formulation, and which is numerically straightforward to apply to complex external flows. The original model coefficients of the k - ϵ model and SSG pressure-strain model remain unaltered, with the exception of consistent modifications based on the new formulation, *e.g.* the increase in C_μ . This demonstrates an eddy-viscosity model formulation constructed primarily from idealized “building-block” flows, such as homogeneous shear, isotropic decay, *etc.*, while still providing predictions commensurate with models calibrated specifically for certain flows. As with all prototypes, there is room for further exploration and improvement to the current model, however the numerical results do suggest that including higher-moment Reynolds-stress information can

improve the predictions for complex flows outside the original model calibration.

Acknowledgments

Thanks to Dr. Michael Rogers of NASA Ames Research Center, and Dr. SolKeun Jee of Oak Ridge Associated Universities, for their helpful discussions and comments on a draft version of the manuscript.

References

- [1] Vassberg, J. C., Tinoco, E. N., Mani, M., Brodersen, O. P., Eisfeld, B., Wahls, R. A., Morrison, J. H., Zickuhr, T., Laffin, K. R., and Mavriplis, D. J., “Summary of the Third AIAA CFD Drag Prediction Workshop,” AIAA Paper 2007-0260, 2007.
- [2] Vassberg, J. C., Tinoco, E. N., Mani, M., Rider, B., Zickuhr, T., Levy, T., Brodersen, O. P., Eisfeld, B., Crippa, S., Wahls, R. A., Morrison, J. H., Zickuhr, T., Laffin, K. R., Mavriplis, D. J., and Murayama, M., “Summary of the Fourth AIAA CFD Drag Prediction Workshop,” AIAA Paper 2010-4547, 2010.
- [3] Oliver, A. B., Lillard, R.P., Schwing, A.M., Blaisdell, G.A., and Lyrantzis, A.S., “Assessment of Turbulent Shock-Boundary Layer Interaction Computations using the OVERFLOW Code,” AIAA Paper 2007-0104, January 2007.
- [4] Childs, R.E., Garcia, J.A., Melton, J.E., Rogers, S.E., Shestopalov, A.J., and Vicker, D.J., “Overflow Simulation Guidelines for Orion Launch Abort Vehicle Aerodynamic Analyses,” AIAA Paper 2011-3163, June 2011.
- [5] Spalart, P.R. and Allmaras, S.R., “A one-equation turbulence model for aerodynamics flows,” *La Recherche Aéronautique*, 1:5–21, 1994.
- [6] Menter, F.R., “Two-Equation Eddy-Viscosity Turbulence Models for Engineering Applications,” *AIAA Journal*, 32(8):1598–1605, 1994.
- [7] Wallin, S. and Johansson, A.V., “An explicit algebraic Reynolds stress model for incompressible and compressible flows,” *Journal of Fluid Mechanics*, 403:89–132, 2000.
- [8] Gerolymos, G.A., Lo, C., and Vallet, I., “Near-wall second moment closure based on DNS analysis of pressure correlations,” AIAA Paper 2011-3574, June 2011.

- [9] Cécora, R.D., Eisfeld, B., Probst, A., Crippa, S. and Radespiel, R., “Differential Reynolds Stress Modeling for Aeronautics,” AIAA Paper 2012-0465, January 2012.
- [10] Lillard, R.P., Oliver, A. B., Olsen, M.E., Blaisdell, G.A., and Lyrantzis, A.S., “The lagRST Model: a Turbulence Model for Non-Equilibrium Flows,” AIAA Paper 2012-0444, January 2012.
- [11] Durbin, P.A., “Near-Wall Turbulence Closure Modeling Without “Damping Functions”,” *Theoretical and Computational Fluid Dynamics*, 3:1–13, 1991.
- [12] Jones, W. and Launder, B., “The prediction of laminarisation with a two equation turbulence model,” *International Journal of Heat and Mass Transfer*, 15(2):301–314, 1972.
- [13] Launder, B. and Sharma, B.I., “Application of an energy-dissipation model of turbulence to the calculation of flow near a spinning disc,” *Letters in Heat and Mass Transfer*, 1(2): 131–138, 1974.
- [14] Durbin, P.A., “Separated Flow Computations with the $k - \epsilon - \bar{v}^2$ model,” *AIAA Journal*, 33(4):659–664, 1995.
- [15] Manceau, R., Carpy, S., and Alfano, D., “A rescaled $\bar{v}^2 - f$ model: First application to separated and impinging flows,” in *Proceedings of the 5th International Symposium on Engineering Turbulence Modelling and Measurements* (Rodi, W. and Fueyo, N., ed.), pp. 107–116, 2002.
- [16] Durbin, P.A., “Application of a near-wall turbulence model to boundary layers and heat transfer,” *International Journal of Heat and Fluid Flow*, 14(3):316–323, 1993.
- [17] Durbin, P.A. and Laurence, D., “Nonlocal effects in single point closure,” in *3rd Advances in Turbulence Research Conference*, pp. 89–90, 1996.
- [18] Lien, F., and Kalitzin, G., “Computations of Transonic Flow with the v^2 - f Turbulence Model,” *International Journal of Heat and Fluid Flow*, 22:53–61, 2001.
- [19] Davidson, L., Nielsen, P.V., and Svingen, A., “Modifications of the v^2 - f Model for Computing the Flow in a 3D Wall Jet,” in *4th International Symposium on Turbulence, Heat and Mass Transfer*, pp. 577–584, 2003.

- [20] Hanjalić, K., Popovac, M., and Hadžiabdić, M., “A robust near-wall elliptic relaxation eddy-viscosity turbulence model for CFD,” *International Journal of Heat and Fluid Flow*, 25:1047–1051, 2004.
- [21] Laurence, D., Uribe, J., and Utyuzhnikov, S., “A robust formulation of the $\bar{v}^2 - f$ model,” *Flow, Turbulence, and Combustion*, 73:169–185, 2004.
- [22] Billard, F. and Laurence, D., “A robust $k - \epsilon - v^2/k$ elliptic blending turbulence model applied to near-wall, separated and buoyant flows,” *International Journal of Heat and Fluid Flow*, 33(1):45 – 58, 2012.
- [23] Adumitroaie, V., Ristorcelli, J.R., and Taulbee, D.B., “Progress in Favré-Reynolds Stress Closures for Compressible Flows,” *Physics of Fluids*, 11(9):2696–2736, 1999.
- [24] Shih, T-H, Zhu, J., and Lumley, J.L., “A new Reynolds stress algebraic equation model,” *Computer Methods in Applied Mechanics and Engineering*, 125:287–302, 1995.
- [25] Bourguet, R., Braza, M., Perrin, R., and Harran, G., “Anisotropic eddy-viscosity concept for strongly detached unsteady flows,” *AIAA Journal*, 45(5):1145–1149, 2007.
- [26] Hamlington, P.E. and Dahm, W.J.A., “Reynolds Stress Closure Including Nonlocal and Nonequilibrium Effects in Turbulent Flows,” AIAA Paper 2009-4162, 2009.
- [27] Moser, R.D., Kim, J., and Mansour, N.N., “Direct numerical simulation of turbulent channel flow up to $Re_\tau = 590$,” *Physics of Fluids*, 11:943–945, 1999.
- [28] Speziale, C.G., Sarkar, S., and Gatski, T.B., “Modelling the pressure-strain correlation of turbulence: an invariant dynamical systems approach,” *Journal of Fluid Mechanics*, 227:245–272, 1991.
- [29] Manceau, R. and Hanjalić, K., “Elliptic blending model: A new near-wall Reynolds-stress turbulence closure,” *Physics of Fluids*, 14(2):744–754, 2002.
- [30] Langer, C.A. and Reynolds, W.C., “A new algebraic structure-based turbulence model for rotating wall-bounded flows,” Center for Turbulence Research Report TF-85, 2003.
- [31] Benton, J.J., “Evaluation of v^2-f and ASBM Turbulence Models for Transonic Aerofoil RAE2822,” in *Progress in Wall Turbulence: Understanding and Modeling*, vol. 14 of *ERCOTAC Series*, pp. 439–450, 2011.

- [32] Durbin, P.A., “On the k - ϵ stagnation point anomaly,” *International Journal of Heat and Fluid Flow*, 17:89–90, 1996.
- [33] Roe, P.L., “Approximate Riemann Solvers, Parameter Vectors, and Difference Schemes,” *Journal of Computational Physics*, 43:357–372, 1981.
- [34] Koren, B., “A robust upwind discretisation method for advection, diffusion and source terms,” in *Notes in Numerical Fluid Mechanics* (Vreugdenhil, C.B. *et al.*, ed.), vol. 45, pp. 117–138, Vieweg, 1993.
- [35] Vandromme, D., “Turbulence modeling for compressible flows and implementation in Navier-Stokes solvers,” VKI Lecture Series 1991-02, 1991.
- [36] Nichols, R.H., Tramel, R.W., and Buning, P.G., “Solver and Turbulence Model Upgrades to OVERFLOW 2 for Unsteady and High-Speed Applications,” AIAA Paper 2006-2824, 2006.
- [37] DeGraaff, D.B. and Eaton, J.K., “Reynolds-number scaling of the flat-plate turbulent boundary layer,” *Journal of Fluid Mechanics*, 422:319–346, 2000.
- [38] Bell, J.H. and Mehta, R.D., “Development of a Two-Stream Mixing Layer from Tripped and Untripped Boundary Layers,” *AIAA Journal*, 28(12):2034–2042, 1990.
- [39] Murman, S.M., “Evaluating Modified Diffusion Coefficients for the SST Turbulence Model Using Benchmark Tests,” AIAA Paper 2011-3571, June 2011.
- [40] Rapp, Ch. and Manhart, M., “Flow over periodic hills: an experimental study,” *Experiments in Fluids*, 51:247–269, 2011.
- [41] Huang, P.G., Coleman, G.N., and Bradshaw, P., “Compressible turbulent channel flows: DNS results and modelling,” *Journal of Fluid Mechanics*, 305:185–218, 1995.
- [42] Zieffle, J., Stolz, S., and Kleiser, L., “Large-Eddy Simulation of Separated Flow in a Channel with Streamwise-Periodic Constrictions,” *AIAA Journal*, 46(7):1705–1718, 2008.
- [43] Cabral, B. and Leedom, L. C., “Imaging vector fields using line integral convolution,” in *Proceedings of the 20th annual conference on Computer graphics and interactive techniques*, SIGGRAPH ’93, (New York, NY, USA), pp. 263–270, ACM, 1993.